

## Atomic iron and nickel in the coma of C/1996 B2 (Hyakutake): production rates, emission mechanisms, and possible parents

S. J. BROMLEY,<sup>1</sup> B. NEFF,<sup>2</sup> S. D. LOCH,<sup>1</sup> J. P. MARLER,<sup>2</sup> J. ORSZÁGH,<sup>3</sup> K. VENKATARAMANI,<sup>1</sup> AND D. BODEWITS<sup>1</sup>

<sup>1</sup>*Department of Physics, Auburn University, Leach Science Center, Auburn, AL 36832, USA*

<sup>2</sup>*Department of Physics and Astronomy, Clemson University, Clemson, SC, 29630, USA*

<sup>3</sup>*Department of Experimental Physics, Faculty of Mathematics, Physics and Informatics, Comenius University in Bratislava, Mlynská dolina F-2, 842 48 Bratislava; Slovak Republic*

(Received TBD; Revised TBD; Accepted TBD)

Submitted to ApJSS

### ABSTRACT

Recently, it has been discovered that gaseous nickel and iron is present in most comets. To evaluate the state of the laboratory data in support of these identifications, we re-analyzed archived spectra of comet C/1996 B2 (Hyakutake), one of the nearest and brightest comets of the last century, using a combined experimental and computational approach. We developed a new, many-level fluorescence model that indicates that the fluorescence emission of Fe I and Ni I vary greatly with heliocentric velocity. Combining this model with laboratory spectra of an Fe-Ni plasma, we identified 23 lines of Fe I and 14 lines of Ni I in the spectrum of Hyakutake. Using Haser models, we estimate the nickel and iron production rates as  $Q_{\text{Ni}} = 2.6 - 4.1 \times 10^{22} \text{ s}^{-1}$  and  $Q_{\text{Fe}} = 0.4 - 2.6 \times 10^{23} \text{ s}^{-1}$ . From derived column densities the Ni/Fe abundance ratio  $\log_{10}[\text{Ni}/\text{Fe}] = -0.38 \pm 0.06$  deviates significantly from solar, and it is consistent with the ratios observed in solar system comets. Spectra from several offset distances show profiles consistent with a short-lived parent and/or emissive photodissociation of an unknown parent species. Possible production and emission mechanisms are analyzed in context of existing laboratory measurements. Based on the observed spatial distributions, excellent fluorescence model agreement, and Ni/Fe ratio, our findings support an origin consisting of dissociation of an unknown parent followed by fluorescence emission. Our findings suggest that the strong heliocentric velocity dependence of the fluorescence efficiencies can provide a meaningful test of the physical process responsible for the Fe I and Ni I emission.

*Keywords:* Laboratory astrophysics (2004), Comets (280), Atomic spectroscopy (2099), Spectral line identification (2073)

### 1. INTRODUCTION

Comets are the remnants of a protoplanetary disk, formed by accretion and preserved in the far reaches of our solar system. Upon transit towards the sun, solar irradiation of the surface sublimates the ices, liberating gas and dust into an expanding cloud known as the coma. Whereas the properties of the nucleus cannot be sampled directly by remote observations, atoms and molecules in the coma enable the study of both the atomic and molecular vestiges of the early solar system. These molecules primarily consist of H, C, N, S, and

O in various formulations (Altwegg et al. 2019). The bulk ices in the nucleus are H<sub>2</sub>O, CO, CO<sub>2</sub>, mixed with other trace species, some of which may reside primarily in the dust (Rubin et al. 2019). Solar radiation photodissociates and photoionizes the molecules, leading to many radicals and atomic fragments (Feldman et al. 2004). Fragment species have many bright emission features in the visible and near-ultraviolet wavelengths, making them an easily accessible proxy to parent species (cf. A'Hearn et al. 1995).

Thus far, the molecular inventory of comets numbers in the dozens, ranging from  $\sim 30$  parent species visible from ground-based observations (Bockelée-Morvan & Biver 2017) and doubling to  $\sim 56$  total *in situ* (cf. 67P, Altwegg et al. 2019). The detection of molecules in

cometary comae sheds light on the abundances and trace organic chemistry during solar system formation.

Metal atoms, on the other hand, are mostly present in refractory materials. They have been discovered in e.g. the sample return mission *Stardust*, which collected dust from comet 81P/Wild 2 and revealed the presence of, among others, copper (Cu), iron (Fe), nickel (Ni), and zirconium (Zr) contained in olivine, sulfides, and other mineral structures (Berger *et al.* 2011; Brownlee 2014). Ca, Fe, K, Li, and Na which are normally absent in Jupiter’s atmosphere were detected after the impact of Shoemaker-Levy 9 (Roos-Serote *et al.* 1995). Neutral and ionized Mg and Fe were detected in UV spectroscopy through meteorites in Mars’ atmosphere after the close encounter with C/2013 A1 (Siding Spring) in Oct. 2014 (Crismani *et al.* 2018). Neutral sodium (Na I) has been detected in several comets, including the tail of comet C/1995 O1 (Hale-Bopp) (Cremonese *et al.* 2002), C/1996 B2 (Hyakutake) (Wyckoff *et al.* 1999), and most recently C/2020 F3 (NEOWISE). These detections summarize the limitations of detecting atomic metals in comets where these endeavors often require extreme events such as close approaches or direct collisions that liberate atoms from within the bulk composition of the nucleus.

In the absence of extreme conditions, detections are even rarer, being limited to sungrazing comets which traverse close to the sun (Jones *et al.* 2017). At one to several AU, temperatures ( $< 300$  K) are insufficient for sublimating refractories or sulfides which require  $T \geq 680$  K (Pollack *et al.* 1994). Sungrazers experience temperatures sufficient for sublimating metal-containing minerals such as olivine  $(\text{Mg,Fe})_2\text{SiO}_4$  that are otherwise inert at the 1 – 3 AU distances common to most spectroscopic studies. The most famous sungrazer to-date was Comet C/1965 S1 (Ikeya-Seki), which passed the sun as close as  $1.7 R_\odot$  (0.008 AU) in 1965. The analyses by Preston (1967) at  $13 R_\odot$  and Slaughter (1969) at  $\sim 30 R_\odot$  revealed lines of Ca I, Ca II, Co I, Cu I, Fe I, K I, Mn I, Na I, Ni I, and V I, from which an effective excitation of 4480 K was derived, suggesting that metal atoms in the coma were excited by fluorescence. Thousands of sungrazers are known, but most are very small, too faint, and/or approach the Sun too closely for spectroscopy (Jones *et al.* 2017).

Most recently, Manfroid *et al.* (2021) reported detections of (gaseous) Fe I and Ni I in the ultraviolet-visible range from a large sample of solar system comets observed with ESO’s Very Large Telescope. Rather fortuitously, the available compilations of atomic data for Fe I and Ni I in the NIST Atomic Spectra Database (hereafter denoted ASD, Kramida *et al.* 2020) are con-

siderable, allowing for development of a detailed many-level atomic fluorescence model. Assuming the emission is driven by fluorescence, Manfroid *et al.* (2021) derived production rates and abundances of both iron and nickel from dozens of emission lines<sup>1</sup>. While the production rates of these species are low ( $\sim$  grams/sec), the large fluorescence efficiencies, owing to the strength of metal emission features in the solar spectrum, enabled their detection.

The molecular parents of these metal atoms are currently unknown. As proposed by Manfroid *et al.* (2021), one possibility is iron and nickel carbonyls, i.e.  $\text{Fe}(\text{CO})_5$  and  $\text{Ni}(\text{CO})_4$ , whose sublimation temperatures are comparable to that of CO (Manfroid *et al.* 2021), which would explain how metallic emission was observed even at large heliocentric distances up to 3.5 AU. Interestingly, these detections are not limited to solar system objects; the interstellar object 2I/Borisov was recently observed by Guzik & Drahus (2021) at 2.3 AU, revealing 9 atomic Ni emission features in the same wavelength window as Manfroid *et al.* (2021). Taken together, it appears that the parents of both metals may be ubiquitous in cometary nuclei and suggest an as-yet-unexplored aspect of organic chemistry (cf. Klotz *et al.* 1996).

In this work, we present a new open-source model of the fluorescence emission of nickel and iron atoms based on atomic data in the ASD. We compare these models to laboratory data of Fe I and Ni I that were acquired as a background measurement for plasma experiments, and archived spectra of C/1996 B2 (Hyakutake) to confirm the line assignments of Manfroid *et al.* (2021) and Guzik & Drahus (2021), add to the inventory of metal lines present in regular cometary spectra, and to evaluate their excitation and formation mechanisms. The fluorescence model is made publicly available to aid future observers.

The remainder of this work is as follows. In Sec. 2, the laboratory spectra of iron and nickel is discussed and an overview of the archived spectra of C/1996 B2 (Hyakutake) is provided. In Sec. 3, the development of a fluorescence model utilizing the full extent of the available laboratory data is discussed. We detail the software implementation of our model, evaluate the propagation of the uncertainties of atomic data through to the synthetic spectra, and benchmark our model against spectra of C/1965 S1 (Ikeya-Seki). In Sec. 4, observed lines of Ni I and Fe I are discussed with special attention on the validity of the identifications. Lastly, in Sec. 5

<sup>1</sup> Line list available as supplementary information at <https://www.researchsquare.com/article/rs-101492/v1>

we compare our production rates and Ni/Fe abundances to previous works and elaborate on complexities of the parent identification.

## 2. DATA

### 2.1. *Experimental data*

The laboratory spectra utilized here were collected during the measurement campaign of Au I and Au II emission reported in Bromley et al. (2020). These experiments used multiple probes containing stainless steel nickel-plated and gold-plated probes from which spectra of gold-iron-nickel plasmas and nickel-iron plasmas were collected. In short, the spectra were collected at resolving power  $\sim 10^4$  between 200 and 800 nm from erosion of the probes inside the Compact Toroidal Hybrid plasma apparatus at Auburn University. A description of the apparatus and optical scheme are available in Hartwell et al. (2017) and Johnson et al. (2019). The nickel spectra acquired in the lab lack emission from the ‘contaminants’ OH, CO, CN, and other volatiles that emit within the 300 - 500 nm window of the comet spectra. However, the lab spectra also show features of H I and neutral and ionized C, N, and O. A detailed analysis of the Ni I and Ni II emission in the lab data will be reported in a future work (B. Neff et al. 2021, in preparation). Though the excitation mechanisms of our plasma experiment are obviously different compared to a comet (electron impact versus photofluorescence), the lab spectra confirm the positions and detections of Ni I emission lines. Electron impact excitation also excites different levels than photofluorescence, allowing us to look for previously undocumented transitions (cf. Bodewits et al. 2019).

### 2.2. *Observations*

The details of the observations, data reduction, and previous analyses of the C/1996 B2 (Hyakutake) spectra are discussed in Meier et al. (1998), Kim et al. (2003), A’Hearn et al. (2013), and A’Hearn et al. (2015a), and the data is available through NASA’s Planetary Data System (A’Hearn et al. 2015b). In summary, the observations of Comet C/1996 B2 (Hyakutake) were acquired on March 26, 1996 using the Echelle Spectrograph on the 4m Mayall Telescope at Kitt Peak National Observatory. The comet was observed with a slit size of  $0.87 \times 7.4$  arcsec where spectra were recorded in the range 300 – 500 nm with resolving power  $\sim 18,000$ . At the time of observation, the comet was traveling at  $-36.7 \text{ km s}^{-1}$  with respect to the sun at a heliocentric distance of 1.02 AU, and only 0.11 AU from Earth. The spectra were wavelength and intensity calibrated using Th-Ar lamps at each echelon order (42 total). The archived spectra were corrected for the wavelength dependent at-

mospheric extinction and A’Hearn et al. (2015b) used spectra of solar analog 16 Cyg B and ‘sky flats’ to remove the continuum caused by sunlight reflected by cometary dust. Wavelength calibrations are accurate to  $\pm 0.02 \text{ nm}$ , and the (relative) intensity calibration within each order is estimated at the 5% level (Meier et al. 1998). However, overfilling of the slit during observations of solar analogs introduces an estimated  $\pm 40\%$  uncertainty on the absolute intensity calibration across the entire wavelength range.

## 3. FLUORESCENCE MODEL

While our laboratory spectra are useful for reporting line positions, the relative line heights cannot be directly compared to comet spectra as the excitation mechanisms are fundamentally different. In our lab plasma, the spectra vary as a function of the electron temperature and density. For a fluorescing media, the spectra is determined by the interplay of absorption, stimulated emission, and spontaneous emission, whose equilibrium balance will change with both heliocentric velocity and distance. A prompt emission origin such as that suggested by Manfroid et al. (2021) would result in populated levels that cannot be achieved through fluorescence. Using a fluorescence model, comparisons of synthetic versus observed spectra reveal clues on the physical process of atomic metal emission in the coma, as well as the chemical origins of these atoms. While one could assume a two-level model to study individual lines driven by absorption from the ground state, atoms with complex electronic structures require a many-level model to properly account for cascades and excited states populated by multiple absorption pathways.

We developed a fluorescence model assuming a collisionless and optically thin environment for the emitted photons, driven by three processes: spontaneous emission (1), stimulated emission (2), and absorption (3). While the rate for (1) is a fundamental property, the rates for (2) and (3) derive from the rate of (1) and the local radiation field at the comet. In the following we outline our fluorescence model; the presentation of the matrices and differential equations is limited to 2 levels for readability.

Consider two levels of a many-level system with a transition from upper level  $j$  to lower level  $i$ . If the Einstein A coefficient for (1),  $A_{j \rightarrow i}$ , is known, the coefficients for (2) and (3) may be expressed as

$$B_{j \rightarrow i} = \frac{\lambda_{ji}^5}{8\pi h c^2} A_{j \rightarrow i} \quad (1)$$

$$B_{i \rightarrow j} = \frac{g_j}{g_i} B_{j \rightarrow i} \quad (2)$$

where  $\lambda_{ji}$  is the (vacuum) wavelength of the transition,  $g_j = 2J_j + 1$ , and  $g_i = 2J_i + 1$ . For each  $B$ , the units [ $\text{m}^3 \text{W}^{-1} \text{s}^{-1}$ ] ensure compatibility with the choice of solar spectrum described later. For a given pair of levels  $j$  and  $i$ , the change in population of the upper state  $j$  is written

$$\frac{dn_j}{dt} = -A_{j \rightarrow i}n_j - B_{j \rightarrow i}\rho(\lambda_{ij})n_j + B_{i \rightarrow j}\rho(\lambda_{ij})n_i \quad (3)$$

with  $B_{ji}$  and  $B_{ij}$  from Eqn's. 1 and 2, and  $\rho(\lambda)$  is the flux per wavelength interval ( $\text{W m}^{-3}$ ) incident on the population  $n_j$  at the energy of the transition from level  $j$  to level  $i$ . The population of the lower state,  $n_i$ , may be written similarly as

$$\frac{dn_i}{dt} = A_{j \rightarrow i}n_j + B_{j \rightarrow i}\rho(\lambda_{ij})n_j - B_{i \rightarrow j}\rho(\lambda_{ij})n_i \quad (4)$$

The above system of equations for levels  $i$  and  $j$  may be written in matrix form as

$$\begin{bmatrix} -\rho_{ij}B_{i \rightarrow j} & A_{j \rightarrow i} + \rho_{ij}B_{j \rightarrow i} \\ \rho_{ij}B_{i \rightarrow j} & -A_{j \rightarrow i} - \rho_{ij}B_{j \rightarrow i} \end{bmatrix} \begin{bmatrix} n_i \\ n_j \end{bmatrix} = \begin{bmatrix} dn_i/dt \\ dn_j/dt \end{bmatrix} \quad (5)$$

In equilibrium, the populations are constant in time and thus the right hand side of Eq. 5 is equal to 0. However, the matrix  $A$  is underdetermined, i.e.  $N$  equations and  $N - 1$  unknowns. We add an additional constraint by enforcing a normalization condition,  $\sum_i n_i = 1$ , by replacing all elements in row 0 of both the left and right matrices by 1. Our matrix equation thus takes the form

$$\mathbf{A}\vec{x} = \mathbf{B} \quad (6)$$

where the rates for processes (1) - (3) are stored in matrix  $\mathbf{A}$  with populations contained within column vector  $\vec{x}$ . Each transition rate contributes to two matrix elements: a positive contribution to the off-diagonal element  $(i, j)$ , and a negative contribution to the diagonal element  $(j, j)$ . Similarly, stimulated emission contributes positively to element  $(i, j)$  and negatively to element  $(j, j)$ . Absorption provides a negative contribution to the diagonal term of level  $i$  at  $(i, i)$ , and an off-diagonal, positive contribution to the population of  $n_j$  in element  $(j, i)$ .

After populating matrices  $A$  and  $B$ , the equilibrium population fractions  $\vec{x}$  follow as  $\vec{x} = A^{-1} \times B$ . The transition intensity, i.e. the fluorescence efficiency of the transition ( $\text{J s}^{-1} \text{particle}^{-1}$ ) at the emitting source from level  $j$  to level  $i$  then follows from the level population  $n_j$  as

$$I_{j \rightarrow i} = \frac{hc}{\lambda_{ji}} n_j A_{j \rightarrow i} \quad (7)$$

where given the directionality of stimulated emission along the sun-comet vector the contribution of stimulated emission to the observed line intensities is assumed to be negligible.

### 3.1. Computational Implementation

We implemented the fluorescence model in Sec. 3 in Python3 and made it publicly available on GitHub<sup>2</sup>. The code requires only standard Python packages, and performs all mathematical operations using NumPy (Harris et al. 2020). SI units are utilized throughout, with conversions indicated where necessary.

First, Einstein  $A$  coefficients, Ritz wavelengths, and level information (energies,  $J$  values) were retrieved from the ASD (Kramida et al. 2020). For each transition, stimulated emission and absorption coefficients follow from Eqns 1 and 2. To generate absorption and stimulated emission rates, we combined computed and measured solar data into a high-resolution solar flux atlas spanning 150 nm - 81  $\mu\text{m}$ . Where possible we have deferred to the measured spectra; however, measurements in the ultraviolet beneath 300 nm and in the infrared beyond  $\sim 1000$  nm are difficult due to substantial atmospheric absorption. Our flux atlas was therefore compiled as follows:

- Between 150 - 199.935 nm, we utilized the high-resolution *computed* flux moments from Kurucz & Bell (1995)<sup>3</sup>,  $F_c(\lambda)$ , from which the flux per wavelength interval in vacuum at 1 AU,  $\rho(\lambda)$ , follows as

$$\rho(\lambda) = 4\pi \times 10^{-3} \left( \frac{R_\odot}{1 \text{ AU}} \right)^2 F_c(\lambda) \quad (8)$$

where  $4\pi \times 10^{-3}$  converts from  $\text{ergs cm}^{-2} \text{s}^{-1} \text{ster}^{-1} \text{nm}^{-1}$  to  $\text{W m}^{-2} \text{nm}^{-1}$  and the radius of the Sun  $R_\odot = 0.00465047 \text{ AU}$ . The model internally converts from  $\text{W m}^{-2} \text{nm}^{-1}$  to  $\text{W m}^{-3}$ .

- Between 199.935 nm and 299 nm, we use the computed flux moments above after conversion to standard air wavelengths using the conversion from Morton (2000).
- Between 299 nm and 1001.27 nm, we utilize the high-resolution solar flux measurements in air ( $\text{W m}^{-2} \text{nm}^{-1}$ ) taken with the Fourier Transform Spectrometer at Kitt Peak National Observatory (Kurucz et al. 1984)<sup>4</sup>. The static choice of

<sup>2</sup> [https://github.com/StevenBromley/fluorescence\\_model](https://github.com/StevenBromley/fluorescence_model)

<sup>3</sup> Available at <http://kurucz.harvard.edu/stars/sun/>

<sup>4</sup> Updated in 2005 and available at <http://kurucz.harvard.edu/sun/irradiance2005/irradthu.dat>

solar spectrum may introduce small errors due to variations in the solar cycle.

- For wavelengths between 1001.27 nm - 81  $\mu\text{m}$ , we utilize the computed flux moments discussed above; wavelengths are treated in vacuum.

Our compiled computed-measured flux atlas is made available in 3 parts (UV, VIS, IR) with our model code and spans  $\sim 150$  nm - 81  $\mu\text{m}$ , is continuous at the boundaries (199.935 nm, 1001.27 nm), and integrates to 1371.64 W/m<sup>2</sup> at 1 AU. If desired, the user is free to import and utilize any radiation field(s), such as those around stars other than the sun for applications such as exocomet studies (Strøm et al. 2020) or handling fluorescence emission of Fe II in active galactic nuclei (Nierenberg et al. 2019; Kovačević et al. 2010). For wavelengths outside the bounds of the solar spectra, the code is capable of assuming a blackbody radiation field, defaulted to 5777 K. Lastly, the flux per wavelength interval  $\rho(\lambda)$  is re-scaled to the comet’s heliocentric distance by a factor of  $1/r_h^2$ .

We tested the sensitivity of our model to the choice of solar spectrum by comparing spectra against those generated using the expanded solar atlas reported in Chance & Kurucz (2010). This atlas extends down to 200 nm (compared to 300 nm above), leading to some line intensities in the range 200 - 300 nm substantially increasing by factors of 100 - 1000. In the range of interest (300 - 500 nm), line intensities typically differ by only  $\sim 20\%$ . However, the poor resolution of this solar spectrum (FWHM 0.5 nm versus  $\sim 0.002$  nm above) makes such a choice likely unsuitable for this application, and we opted to use the high-resolution compiled spectrum discussed previously.

We also investigated the necessity of utilizing a line profile over which the solar spectrum is absorbed. For the heavy elements (nickel, iron) of interest, both Doppler and Lorentzian line profiles are negligibly small with respect to the resolution of the solar spectrum, and we use (effectively) a delta function line profile.

When calculating the absorption and stimulated emission rates,  $W = \rho(\lambda_{ij})B$ , the Doppler shift of the solar spectrum resulting from the comet’s heliocentric velocity (-36.7 km/s during the archived observations of Hyakutake) is included. After the initial matrix population, the inverse of the rate matrix ( $A^{-1}$ ) is calculated using the NumPy `linalg.inv` package, from which the populations follow as  $\vec{x} = A^{-1} \times B$ . For large singular or near-singular matrices caused by missing atomic data or small heliocentric distances (i.e. large absorption rates), the code attempts a solution using a Pseudo-Inverse (`linalg.pinv`) and Singular Value Decomposi-

Flag	Uncertainty(%)	# Ni	# Fe
AAA	$\leq 0.3$	0	0
AA	$\leq 1$	0	0
A+	$\leq 2$	0	0
A	$\leq 3$	0	149
B+	$\leq 7$	0	282
B	$\leq 10$	0	622
C+	$\leq 18$	56	509
C	$\leq 25$	126	205
D+	$\leq 40$	45	188
D	$\leq 50$	211	191
E	$> 50$	84	393

**Table 1.** Einstein  $A$  value accuracy scale in the NIST Atomic Spectra Database (Kramida et al. 2020). The number of lines with each rating for Ni I and Fe I are shown.

tion (`linalg.svd`). From the equilibrium populations, line intensities are calculated using Eq. 7, and vacuum wavelengths are doppler-shifted by the geocentric comet velocity before conversion to standard air wavelengths using the conversion of Morton (2000). We note that for the observation of C/1996 B2 (Hyakutake) utilized here the geocentric velocity was effectively 0 km/s, and the observation was recorded for  $\Delta = 0.11$  AU.

Lastly, our model code directly imports the line and level lists which are downloaded from the ASD, and can thus be used to analyze any neutral or ionized atomic species for which the requisite data is available.

### 3.2. Error Propagation

The Einstein  $A$  values were sourced from the ASD (Kramida et al. 2020) in which each  $A$  value is assigned an accuracy rating by NIST. The ASD  $A$  value accuracy scale is shown in Table 1, and spans from  $\leq 0.3\%$  to  $> 50\%$ . Though some  $A$  values used in our model may have large uncertainties in excess of 50%, line intensities from the model cannot simply be attributed an uncertainty equal to that of the  $A$  value. For each transition, the 6 resulting contributions to the rate matrix each modify the detailed balance which determines the equilibrium populations. Therefore, we adopted the following Monte-Carlo procedure for approximating the *uncorrelated* uncertainties of the model intensities from the  $A$  value uncertainties.

Error bars on model intensities are derived by looking at changes in line intensities following the simultaneous adjustment of all  $A$  values. For each iteration,  $A$  values are randomly and uniformly varied within a range of  $\pm$  the accuracy rating e.g.  $\pm 10\%$  for ‘B’ ratings. For the lowest accuracy rating (E,  $>50\%$ ), we allow variations up to  $\pm 100\%$ . We calculate the error bar for each

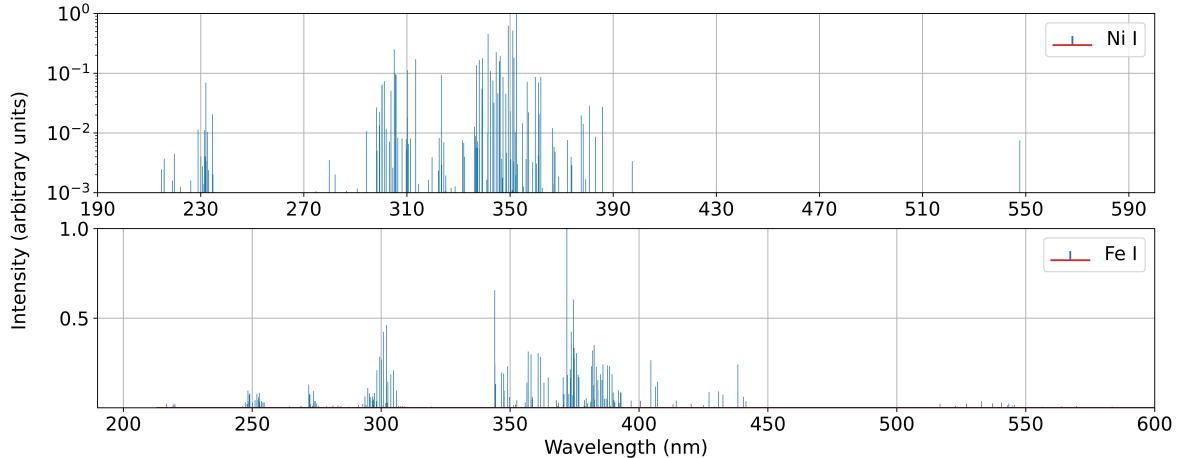


**Figure 1.** Synthetic fluorescence spectra stick plot on a logarithmic intensity scale with the strongest lines normalized to 1 for Ni I (top) and Fe I (bottom) spanning 190 - 600 nm. Line intensities were calculated for the observing conditions of C/1996 B2 Hyakutake,  $v_h = -36.7$  km/s and  $r_h = 1.02$  AU.

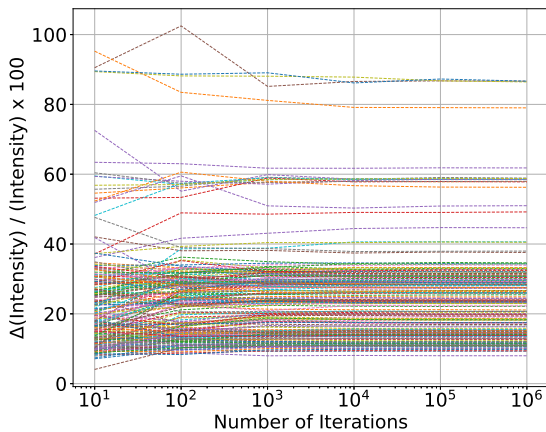


**Figure 2.** Ratio of line intensity standard deviation to line intensity (in percentage) for 213 Ni I lines spanning 300 - 500 nm as a function of iteration number (see text). Spectra were generated at the orbital conditions of the closest approach of C/1996 Hyakutake and are plotted at  $10^1$ ,  $10^2$ ,  $10^3$ ,  $10^4$ ,  $10^5$ , and  $10^6$  iterations. Each colored line shows the convergence of an individual transition.

emission line,  $\Delta I_{j \rightarrow i}$ , as the standard deviation of the line intensity across all iterations. We note that this is likely an overestimate of the uncorrelated uncertainty, as a Gaussian distribution (compared to the present uniformly distributed uncertainties) would favor lower variations for each  $A$  value adjustment.

### 3.3. Ni I Model

For Ni I, the 522 transitions in the ASD were incorporated into our fluorescence model, involving 133 of the 288 known levels. For the 155 excluded levels, no tran-

sitions with transition rates were available. A synthetic spectra of Ni I at 1.02 AU and a heliocentric velocity  $v_h = -36.7$  km/s is shown in Fig. 1 (top). The strongest emissions are between 300 - 390 nm. The model also suggests possibly-observable emission (from space-based missions) around  $\sim 230$  nm, but this emission is outside the bandpass of the archived spectra of Hyakutake. For Hyakutake, the expected strongest emission overlaps with the wavelength ranges wherein nickel emission was identified by Manfroid *et al.* (2021) and Guzik & Drahus (2021).

We derived error bars for the Ni I lines by iterating our Monte-Carlo procedure with  $10^n$  ( $n = 0 - 6$ ) iterations at the observing conditions of C/1996 B2 (Hyakutake). Fig. 2 shows the convergence of our method with increasing number of iterations; only lines in the range 300 - 500 nm are shown for visibility. The majority of the standard deviations converge by  $10^4$  iterations, which requires  $\sim 20$  minutes of compute time on a modern personal computer.

Fig. 3 (top) shows the ratio of model standard deviation to model line intensity (in percentage) versus the NIST stated uncertainty rating (percentage) following  $10^6$  iterations for selected lines of Ni I. The dashed red line  $y = x$  is plotted as a visual aid only. ‘Strong’ lines (black) are those with a model uncertainty with an intensity within a factor of 10 of the strongest line. ‘Moderate’ lines (red) are those with  $10 < I_{\text{strongest}}/I_{\text{line}} < 100$ , and ‘weak’ lines (blue) are those with  $100 < I_{\text{strongest}}/I_{\text{line}} < 1000$ . A total of 134 lines meeting these criteria are shown.

The remaining (not shown) lines are very weak and exhibit large model uncertainties. We note that the 84

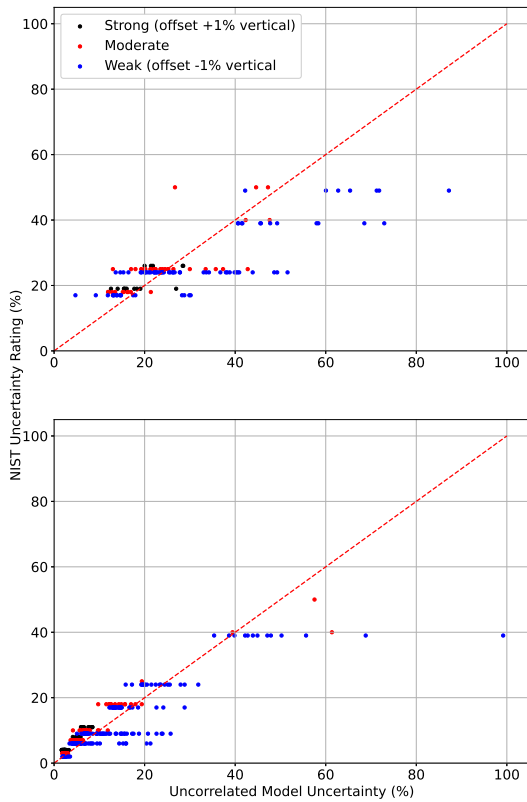


**Figure 3.** (Top) Model uncertainties for the fluorescence spectrum of Ni I, calculated as the standard deviation of line intensities following  $10^6$  iterations within the limits of  $\pm$  ASD Accuracy (see Table 1) versus the ASD accuracy rating for 134 selected transitions with model uncertainties  $< 100\%$ . Strong lines (15 total) are considered as those with intensities within a factor of 10 of the strongest line. Moderate lines (39) and weak lines (80) are considered as those within factors of 100 and 1000 of the strongest line intensity, respectively. Strong and weak lines are offset  $\pm 1\%$  vertically for visibility. (Bottom) Fe I model uncertainties versus ASD accuracy ratings for 381 select transitions with uncertainties lower than  $100\%$ : 54 strong, 116 moderate, and 211 weak.

‘E’-rated lines all present significant sensitivity to our Monte-Carlo procedure and exhibit extremely large uncertainties in excess of  $10^8\%$ , owing to floating point errors and/or extremely small level populations. Thirty-nine of these 84 lines are E2 transitions between even-parity configurations where the upper levels are weakly populated by fluorescence; the dominant source of their population is absorption from the (already low) populations of excited odd parity states. Twenty-one separate ‘E’-rated transitions are from excited even configura-

tions to the excited odd configurations, and suffer from a similar limitation. The remaining 24 ‘E’-rated transitions are outside our region of interest (300 - 500 nm).

For weak lines, the small scales of both level populations and fluorescence efficiencies presents computational difficulties. For possible future investigations of particular lines using our model, it may be appropriate to investigate the model’s sensitivity to changes in particular lines within some constraint e.g. the effect of branching ratio uncertainty for a particular upper level. However, such an investigation is outside the scope of this work.

In general, we find the Monte-Carlo procedure sufficient for approximating the sensitivity of strong lines to the uncertainties of the transition rates. For strong and moderately strong lines, the model uncertainty is comparable to or less than the stated ASD uncertainty rating. The reason for this is likely due to the following: recall that for a two-level system the populations follow as

$$n_2 = n_1 \frac{W_{1 \rightarrow 2}}{W_{2 \rightarrow 1} + A_{2 \rightarrow 1}} \quad (9)$$

where  $W_{1 \rightarrow 2}$  is the absorption rate,  $W_{2 \rightarrow 1}$  is the stimulated emission rate, and  $A_{2 \rightarrow 1}$  is the spontaneous emission rate. By definition, the Einstein B coefficients are proportional to the A value, and the net effect of an increase in A, e.g.  $A \rightarrow 2 \times A$  propagates through the B coefficients and leaves the ratio  $n_2/n_1$  unchanged. However, the change in A value propagates through the intensity from Eq. 7 as  $I_{2 \rightarrow 1} \propto A_{2 \rightarrow 1}$ , and thus the A value uncertainty is the intensity uncertainty.

For a many-level system, we find that intensities for levels that are well-connected and well-populated are less affected by changes in A values compared to levels connected by fewer transitions as the changes in multiple A values partially cancel. For levels with one or few connections to the bulk of the levels, the uncertainty of the A value more directly propagates through to the uncertainty of the line intensity. Given the scale of the Ni I rate matrix,  $133^2$  possible elements populated by  $522 \times 6 = 3132$  rates, the A value iterations for well-populated levels (which thus produce the strongest lines) are effectively a perturbation. In this case, the quantity of atomic data, assumed to accurately reflect the totality of the level structure, including all important transitions, acts as a buffer against large fluctuations in model outputs for the strongest lines.

### 3.4. Fe I Model

For Fe I, we included the 2542 transitions with transition rates in the ASD, involving a total of 434 levels. Though more than 50% of the transitions are outside

our spectral window, they may affect the level populations and were included. Our flux atlas was sufficient for producing absorption and stimulated emission rates for all but one line; the solar flux for the M1 line at  $111.18 \mu\text{m}$  ( $3d^6 4s^2 \ ^5D_0 \rightarrow 3d^6 4s^2 \ ^5D_1$ ), though negligible, was approximated with a blackbody at 5777 K.

Fig. 1 (*bottom*) shows synthetic Fe I fluorescence spectra at the observing conditions of comet Hyakutake (Meier *et al.* 1998). The strongest lines are predicted in the UV between  $\sim 340 - 390 \text{ nm}$ . For the Fe I Monte-Carlo iterations, the error bars of most lines ( $> 99\%$ ) converge within  $10^4$  iterations. In Fig. 3 (*bottom*), we show a comparison of our Monte-Carlo uncertainty calculation versus the NIST accuracy ratings of the transition rates for 381 selected lines following the procedure derived for Ni I. Compared to Ni I, most of the strongest lines of Fe I exhibit a Monte-Carlo uncertainty less than the ASD accuracy rating. For relatively weak lines, the Monte-Carlo uncertainty typically exceeds the ASD uncertainty rating.

### 3.5. Total Model Uncertainties

For the archived data of C/1996 B2 (Hyakutake), the heliocentric velocity ( $-36.7 \text{ km/s}$ ) leads to favorable fluorescence efficiencies. Within a range of  $\pm 1 \text{ km/s}$  the average change in fluorescence efficiencies for all lines was 9% for Ni I and 4% for Fe I. Our total model uncertainties were obtained by adding in quadrature the uncertainty of the converged Monte-Carlo iterations and the average deviation over a 200-point grid of models spanning  $v_h \pm 1 \text{ km/s}$ .

### 3.6. Benchmarking Against Sungrazer Ikeya-Seki

As an additional check on the accuracy of the fluorescence model, we applied our model to the spectra of Fe I and Ni I collected during the perihelion passage of comet Ikeya-Seki in 1965. Two line lists are available from Slaughter (1969) at  $30 R_\odot$  ( $v_h \sim 154 \text{ km s}^{-1}$ ) and Preston (1967) at  $\sim 13 R_\odot$  ( $v_h \sim 116 \text{ km s}^{-1}$ )<sup>5</sup>

Fig. 4 shows the comparison of our model spectra and intensities of Fe I and Ni I lines reported by Slaughter (1969) and Preston (1967). The spectra were first multiplied by a constant to place the model intensities on the same approximate scale, then re-scaled via a linear fit of observed versus model intensity. The Ikeya-Seki spectra were recorded on photographic plates, and thus a direct comparison between the model versus observed intensities is difficult. Slaughter (1969) notes that agreement between expected and observed line intensities of

a thorium-argon lamp agreed within a factor of 2. Preston (1967) reported intensities in terms of the local sky continuum, and thus we expect their intensity scale may differ as a function of wavelength. We assume a similar factor of 2 scatter due to intensity calibration.

The best agreement between our model and the reported lines in the spectra of Ikeya-Seki is found for the spectra collected at  $13 R_\odot$  by Preston (1967). The agreement with all observations, particularly the spectra from  $30 R_\odot$  (Slaughter 1969), is improved significantly if a linear offset is included in the fit (assumed to account for reflected solar continuum). The large thermal temperature ( $T > 4000 \text{ K}$ ) in Ikeya-Seki may have introduced additional emission from thermal excitation, but this effect would be more pronounced for the spectra of Preston (1967). The source of the disagreement between our model and the line list of Slaughter (1969) is not known. However, lines that were strong in the Ikeya-Seki spectra have appreciable intensities in our models, and we thus consider this agreement as sufficient validation of our model.

### 3.7. Molecular Contamination

NUV and optical cometary spectra consist of reflected sun light superimposed on many emission features of radicals. To determine the reliability of our line identifications, we used the Planetary Spectrum Generator (PSG) to generate synthetic fluorescence spectra of the diatomic molecules OH, CN,  $\text{C}_2$ , NH, and CH (Villanueva *et al.* 2018). We note that the emission of neither metals, triatomics (e.g.  $\text{C}_3$ ), or prompt emission of OH are presently available in the PSG. Spectra were generated for production rates set to unity, which were then re-scaled by the rates measured by Meier *et al.* (1998) and Schleicher & Osip (2002). The molecular spectra were then manually re-scaled to approximately match our comet spectra. This procedure is not intended to accurately replicate the exact features in our comet spectra, but to elucidate sources of contamination in identified metallic lines. The molecular features are well spread across the orders of the echelle and make apparent the uncertainty of the wavelength calibration around some of the metallic features.

To aid future spectroscopy efforts, we have defined the following confidence scale for our line identifications. ‘A’ ratings are stated for isolated lines with no strong nearby features and whose line profile is well fit. ‘B’ ratings are listed for lines with one or more flaws, including possible molecular contamination or blends in the lab spectra. Lastly, ‘C’ ratings are listed for lines with serious molecular contamination, poor fit, or small signal-to-noise. For each letter grade, additional flags

<sup>5</sup> <https://ssd.jpl.nasa.gov/horizons.cgi>

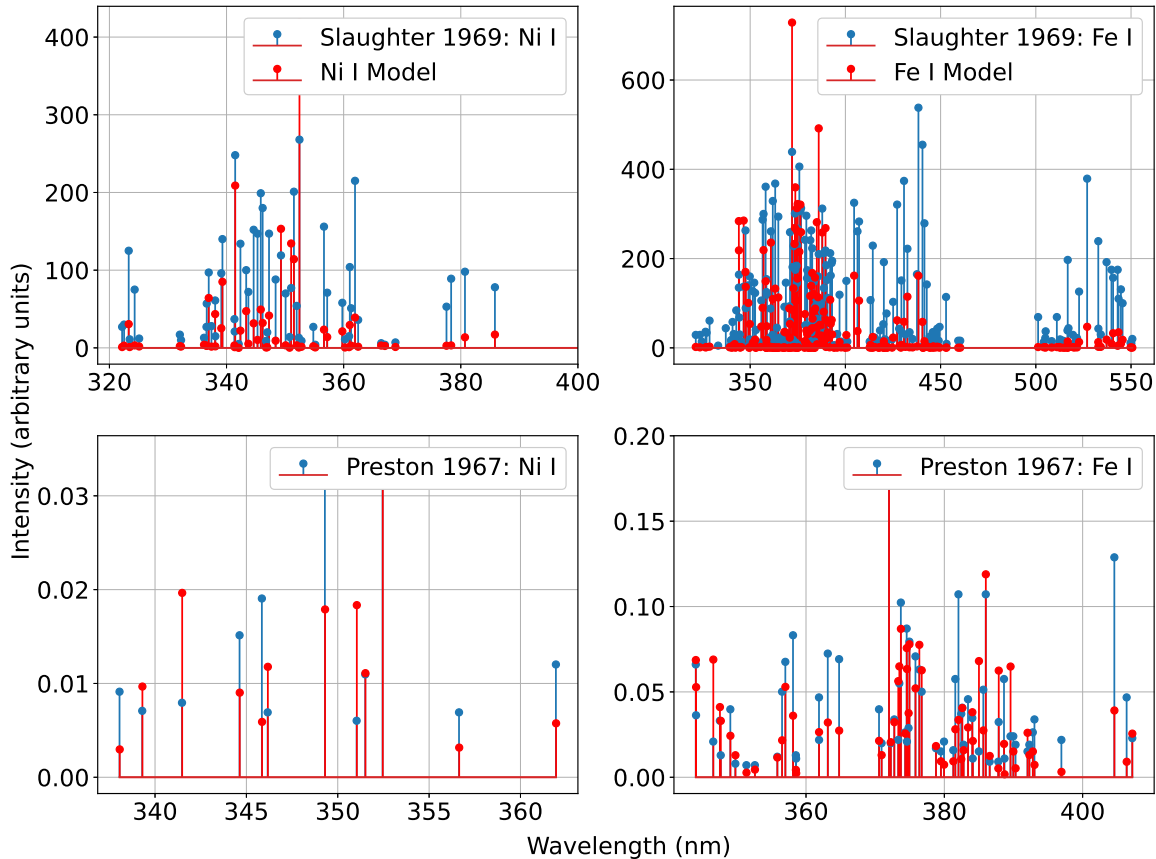


**Figure 4.** Comparison of Ni I (left) and Fe I (right) line intensities of our fluorescence model to the observed intensities of comet Ikeya-Seki as reported in Slaughter (1969) (top) and Preston (1967) (bottom). The model spectra are scaled via a linear fit of all present lines.

are shown in parentheses indicating the source of the molecular contamination e.g. (CN).

## 4. RESULTS

### 4.1. Detections of Ni I and Fe I lines

The metal lines from atomic iron and nickel we identified in the spectrum of Hyakutake are listed in Table 2. Where possible, we have indicated if a line has previously been observed by Manfroid et al. (2021), Guzik & Drahus (2021), or in the spectra of Ikeya-Seki (Slaughter 1969; Preston 1967). Ritz, comet, and lab wavelengths, observed and modeled intensities, upper/lower configuration information, and confidence ratings are also provided.

In general, we identified 14 Ni I emission lines by comparison with the fluorescence model and lab spectra. Within these 14 lines, 13 were found in both the lab and comet spectra, with the remaining line identified by

comparison with our model exclusively. In some cases, deviations between the known air wavelengths of the observed lines and their wavelength in the comet spectra are  $\sim 0.02$  nm. These wavelength differences were noted by A’Hearn et al. (2015a) as resulting from calibration of the numerous orders of the echelle spectrograph. However, the direction and scale of the wavelength shift(s) are obvious when comparing heights and positions of several nearby metal and/or molecular features.

Fig. 5 shows a comparison of a region of the comet spectra containing many features of atomic nickel. Lab spectra are overlaid and scaled to the Ni I line at 345.85 nm. The nickel model is scaled to the 345.85 nm nickel feature and shown as red vertical lines. After this initial scaling the Ni I lines identified by Manfroid et al. (2021) and Guzik & Drahus (2021) are readily apparent in the spectra of Hyakutake. A total of 28 Ni I lines were reported by Manfroid et al. (2021), 14 of which

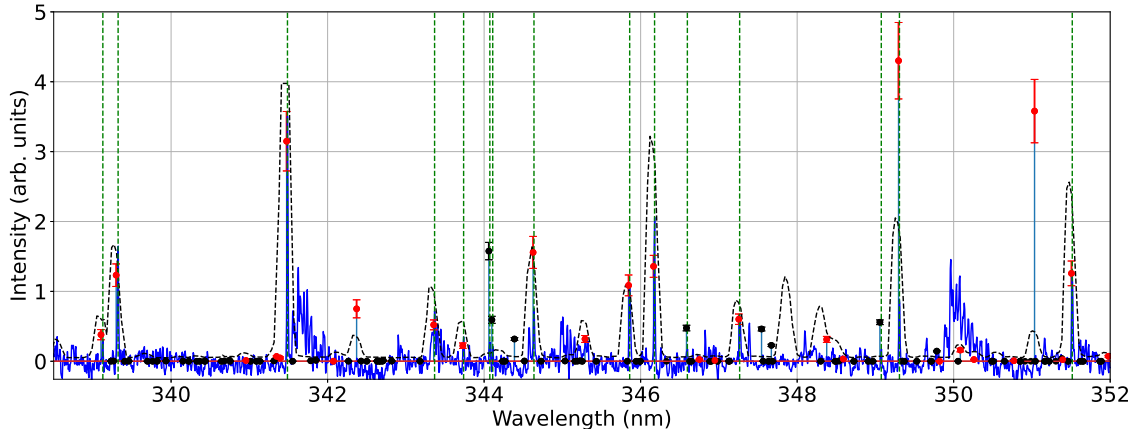


**Figure 5.** Comparison of lab spectra (dashed black), comet spectra (solid blue), the Ni I fluorescence model results (red), and the Fe I fluorescence model (black); confirmed lines are indicated by dashed green vertical lines. Error bars on the model intensities are from the  $10^6$  iterations described in Sec. 3.2 added in quadrature with the standard deviations derived from a grid of models spanning  $v_h \pm 1$  km/s; lines with very large uncertainties driven by low level populations are omitted for clarity. The line heights for the model and lab spectra were normalized to the Ni I line at 345.86 nm; the Fe I fluorescence model is normalized to the strong 371.99 nm iron line (not shown). The lab spectra are shifted +0.04 nm to enhance visibility of the underlying peaks in the comet spectra. The lab spectra shown are from CTH shot 18112918, frame 85.

were observed in our comet spectra. The nine lines of Ni I observed in 2I/Borisov by Guzik & Drahus (2021) were all present in the spectra of Hyakutake.

We identified a total of 23 Fe I lines in the spectrum of Hyakutake, 22 of which were also in the line list of Manfroid *et al.* (2021). The additional line was found in Ikeya-Seki, and is among the weakest iron features in our spectra. The non-detection of this line in the sample of Manfroid *et al.* (2021) is not surprising given Hyakutake’s proximity to Earth ( $\Delta = 0.11$  AU), large activity ( $Q_{\text{H}_2\text{O}} > 10^{29}$  mol.  $\text{s}^{-1}$ , Meier *et al.* 1998) and favorable heliocentric velocity. We note that every metal line detected in Hyakutake was observed in Ikeya-Seki.

Only 10 (43%) of the comet’s Fe I lines were also identified in the lab spectra, though many more Fe I and Fe II features are apparent in the range 200 – 300 nm in the lab spectra. This is not so surprising; before iron is eroded into the plasma, the nickel layer must be worn away to expose the stainless steel probe underneath. Similarly, the higher temperature ( $T_e > 20$  eV) leads to a significant population of Fe II. We note that in the comet spectra, Fe I lines are generally weaker than those of Ni I, and we find no evidence of Fe II (cf. Sec. 4.2).

Our observed metal emission lines are dipole-allowed transitions from the excited odd configurations of the form  $3d^x 4p$  and  $3d^x 4s 4p$  to the ground and metastable configurations  $3d^x 4s$  and  $3d^x 4s^2$ . In Fig. 6 we show Grotrian diagrams of Ni I and Fe I where observed transitions are indicated by diagonal red lines. We find no evidence of population of any states which cannot be explained by absorption from the ground or metastable

levels; the spectrum is fully consistent with fluorescence of atomic Ni and Fe. In total, we find agreement between our modeled fluorescence efficiencies and the observed line intensities of the identified metal features. For both nickel and iron we find the model and comet intensities agree on average within a factor of  $\sim 2$ .

According to our fluorescence model, the populations of the first 6 levels of Ni I above ground have populations comparable to the ground state, giving rise to two possible IR transitions at 3119 nm ( $3,205.15$   $\text{cm}^{-1}$ ) and 7506 nm ( $1332.164$   $\text{cm}^{-1}$ ) with fluorescence efficiencies comparable to the strong UV-optical transitions observed here. Similarly, the metastable levels of Fe I have not-insignificant populations, but no significant emission in the infrared is predicted by our model.

#### 4.2. Searches for Other Metal Emission

In addition to neutral iron and nickel, we searched for Fe II and Ni II; no matches in both wavelength and model intensity were found. We also searched for lines belonging to neutral and singly ionized metals present in Ikeya-Seki and dust grains: Al, Ca, Co, Cr, Cu, Mg, Mn, Na, Zn, and V. Searches for Na emission were hopeful considering the detection of the (weak) Na I doublet at 589 nm in the tail of comet Hyakutake by Wyckoff *et al.* (1999). However, fluorescence efficiencies of Na lines in our wavelength window are a factor of 10 - 100 weaker than the sodium doublet and the lines were undetectable in our spectra. No matches were found for both wavelength and relative intensity of the other elements listed above.

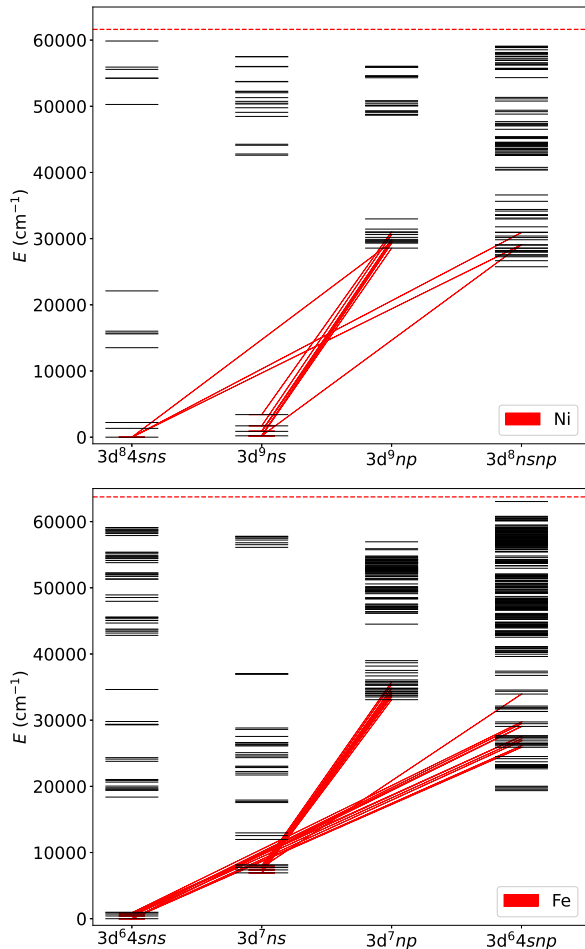


**Figure 6.** Grotrian diagrams of Ni I (top) and Fe I (bottom) showing the observed emission lines of each element as diagonal red lines. Ionization limits are shown as horizontal dashed lines. Many lines are known for each element (522 for Ni, 2539 for Fe) but only the observed lines are shown for clarity.

We draw attention to a particularly strong and sharp line at 416.68 nm for which no emission lines produced by our models were an appropriate match. Comparisons to data in the ASD suggest V I or Cu II, but these two transitions lack  $A$  values and both are between excited states, i.e. they are likely weak at 1 AU. A possible (prompt) molecular origin is NH, though the transition rate for this particular transition is weak (Fernando et al. 2018).

#### 4.3. Production Rates and Abundances

Spectra were taken at various spatial offsets in the Hyakutake observations of Meier et al. (1998), but there is great uncertainty in photocenter location with respect to the nucleus for each offset observation. We opted to focus our analysis on the centered observa-

tion and calculate aperture-averaged column densities. Our fluorescence efficiencies  $I_{ij}$  are calculated in units of  $\text{J s}^{-1} \text{ particle}^{-1}$  at the emitting source; the conversion from observed flux ( $\text{J cm}^{-2} \text{ s}^{-1} \text{ nm}^{-1}$  integrated over a gaussian fit) to column density follows as

$$F_{ij} = \frac{A_{\text{ap.}}}{4\pi\Delta^2} I_{ij} n_{\text{col.}} \quad (10)$$

where  $F_i$  is the observed cometary flux from line  $\lambda_{ij}$ ,  $A_{\text{ap.}}$  is the sky projected slit size ( $68 \times 580 \text{ km}^2$ ),  $\Delta$  is the geocentric distance,  $I_{ij}$  is the calculated fluorescence efficiency (Eq. 7), and  $n_{\text{col.}}$  is the column density. In Fig. 7 we show the comparison of modeled and observed line intensities for both nickel and iron. From weighted fits (dashed lines, calculated with `scipy.odr`, cf. Virtanen et al. 2020) of model versus the distance-scaled model intensity the column densities of neutral nickel and iron follow from the slopes as  $n_{\text{Ni}} = 6 \pm 1 \times 10^9 \text{ cm}^{-2}$  and  $n_{\text{Fe}} = 14.7 \pm 0.7 \times 10^9 \text{ cm}^{-2}$ .

As the observed spectra are well described by fluorescence, we expect a consistent outflow velocity for all nickel and iron atoms. Assuming a gas expansion velocity of  $v = 0.85 R_{\text{h}}^{-1/2} \text{ km s}^{-1}$  (Cochran & Schleicher 1993), we calculate the production rate of these metal atoms using Haser models (see the recent translation in Haser et al. 2020) implemented in the Small Body Python (`sbpy`) code (Mommert et al. 2019). The use of a Haser model to derive production rates in this context requires several assumptions. For species produced via dissociation or fragmentation (as expected for nickel and iron), each fragment receives a velocity kick (distribution) which may result in a higher outflow velocity than that derived from the assumed relation above. Presently, the production mechanisms and possible parent loss mechanisms are unknown, and application of a vectorial model (Festou 1981) would not improve the accuracy of our results.

We have attempted to minimize the inaccuracies of our Haser models by restricting our parameter space and deriving daughter scalelengths from known photoionization rates of nickel and iron. Using the known lifetimes at 1 AU from the Sun during solar minimum for Ni I ( $1.06 \times 10^6 \text{ s}$ ) and Fe I ( $5.94 \times 10^5 \text{ s}$ ) (Huebner & Mukherjee 2015), we derived daughter scalelengths of  $8.92 \times 10^5 \text{ km}$  and  $5.01 \times 10^5 \text{ km}$  respectively. For the unknown parent, we restricted the scalelength to  $l_{\text{parent}} < 1000 \text{ km}$  in line with the model work of Guzik & Drahus (2021).

Without additional spatial information, we are limited to restricting the production rate to a range within the bounds calculated from the uncertainty of the observed total numbers of particles. We iterated the Haser models over a grid of parent scalelength and production rate,

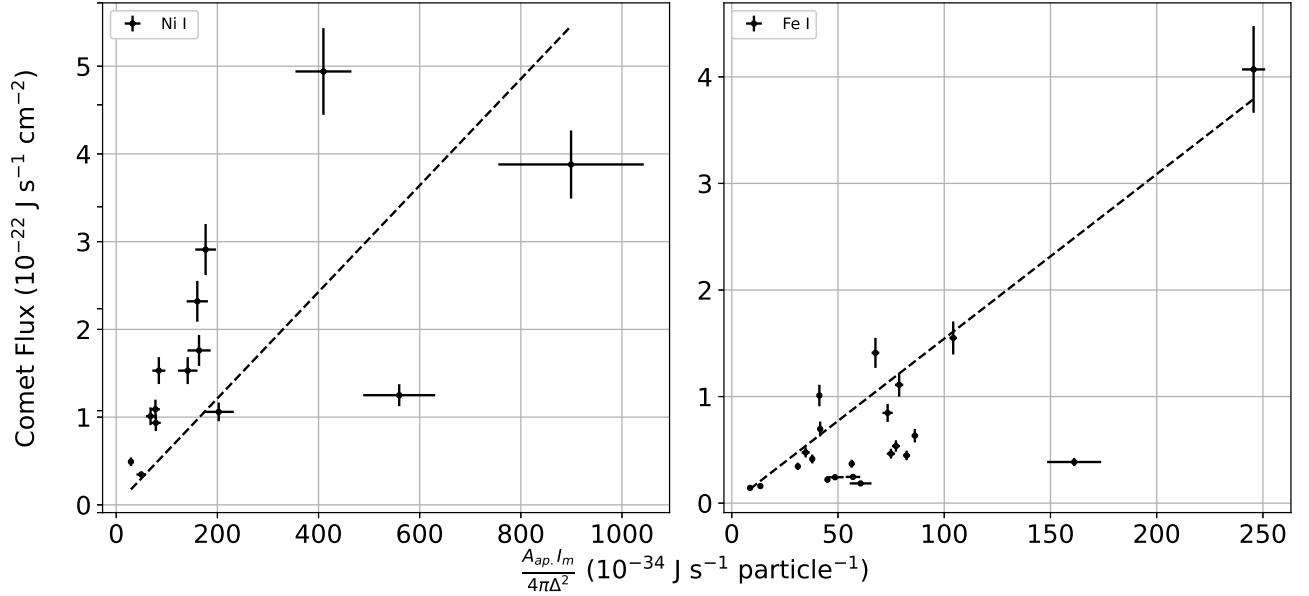


**Figure 7.** Comparison of model and observed line intensities of Ni I (left) and Fe I (right). Model error bars are taken as the quadrature sum of the Monte-Carlo uncertainty and the sensitivity to heliocentric velocity (see text), and an absolute error for the observed intensities was assumed to be  $\pm 40\%$  (Meier et al. 1998). The weighted fits are shown as dashed lines respectively.

after which the Haser column densities were integrated over the rectangular aperture. Using the observed total number of particles within our aperture ( $N = A_{\text{ap.}} \times n_{\text{col.}}$ ,  $N_{\text{Ni}} = 2.4 \pm 0.4 \times 10^{24}$ ,  $N_{\text{Fe}} = 6.1 \pm 0.3 \times 10^{24}$ ), we narrowed the range of production rates for nickel and iron to  $Q_{\text{Ni}} = 2.7 - 4.1 \times 10^{22} \text{ s}^{-1}$  and  $Q_{\text{Fe}} = 0.4 - 2.6 \times 10^{23} \text{ s}^{-1}$ .

## 5. DISCUSSION

### 5.1. Comparison of Hyakutake to the broader sample of comets

Due to their large fluorescence efficiencies, neutral iron and nickel emission were observed for production rates as low as  $\sim 8 \times 10^{21} \text{ s}^{-1}$  by Manfroid et al. (2021). Our production rates are comparable to those observed in other solar system comets in order  $\sim 10^{22} \text{ s}^{-1}$  with the large uncertainties stemming from the lack of spatial information and intensity calibration of our echelle spectra. Hyakutake was a particularly active comet with  $Q_{\text{H}_2\text{O}} > 2.2 \times 10^{29} \text{ mol. s}^{-1}$  (Meier et al. 1998), and our iron production rate is comparable to the most active comet observed by Manfroid et al. (2021), C/2016 R2 (PANSTARRS). The nickel production rate in Hyakutake is in-line with the majority of the already observed solar system comets.

The Ni/Fe abundance ratios reported for solar system comets (in  $\log_{10}$ ) spans the range  $-0.68$  to  $+0.6$ . From our production rates, the Ni/Fe abundance observed in

Hyakutake (in  $\log_{10}$ , hereafter denoted [Ni/Fe]) ranges from  $-0.98$  to  $0.01$ . This range is dominated by additional uncertainties introduced via the lack of constraint on parent scalelength in the present work. In this context, it is more appropriate to derive a [Ni/Fe] abundance from the column densities which yields [Ni/Fe] =  $-0.38 \pm 0.06$ . This Ni/Fe abundance differs significantly from both solar ( $-1.25$ ) and Ikeya-Seki ( $-1.11$ ) ratios where the fluorescing material is sourced from the bulk composition, and from dust collected from 1P (Halley) where  $\log(\text{Ni/Fe}) = -2.5$  (Jessberger et al. 1988). This finding is consistent with the proposition of Manfroid et al. (2021) that the Ni and Fe are produced by dissociation of an intermediate parent instead of sublimating dust.

Fig. 8 shows a comparison of abundance ratios in Hyakutake (dashed red lines) to comets studied by Manfroid et al. (2021) and Guzik & Drahus (2021). Abundance ratios for Hyakutake were derived from the mean production rates of the ranges specified previously and are shown as dashed vertical red lines. Abundance ratios for 2I/Borisov are shown as dashed black lines where applicable. Hyakutake appears relatively depleted in Ni with respect to both OH and CN. Using our mean Fe production rate ( $1.5 \times 10^{23} \text{ s}^{-1}$ ), Hyakutake’s Fe/OH and Fe/CN abundances are similar to the majority of solar system comets.

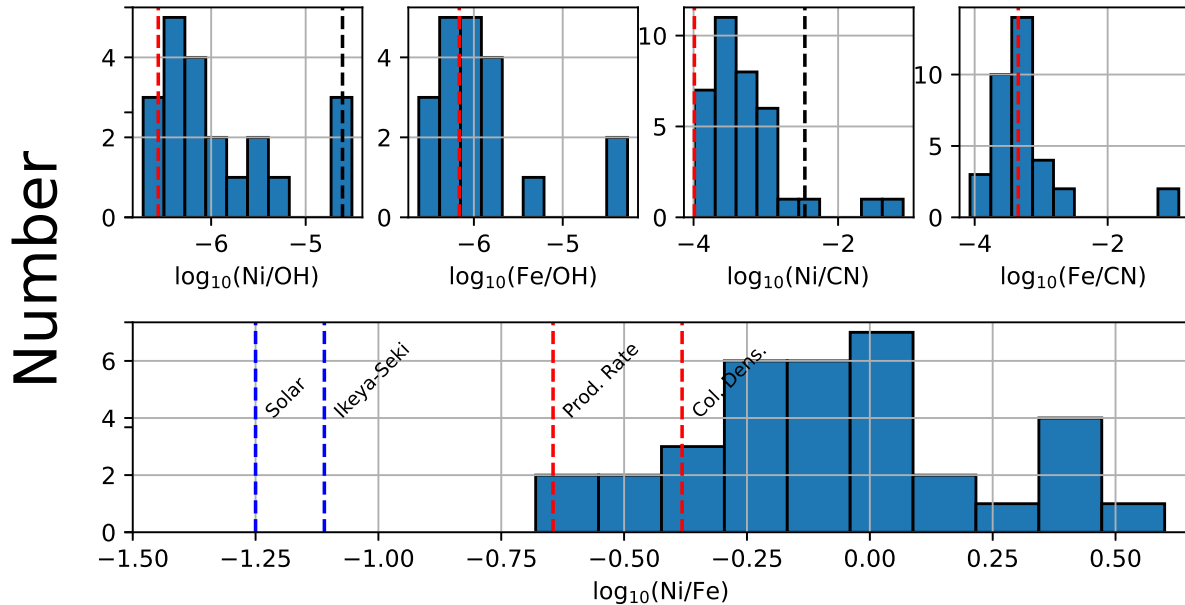


**Figure 8.** Histograms ( $\#$  bins = 10) of  $[\text{Ni}/\text{OH}]$ ,  $[\text{Fe}/\text{OH}]$ ,  $[\text{Ni}/\text{CN}]$ ,  $[\text{Fe}/\text{CN}]$ , and  $[\text{Ni}/\text{Fe}]$  in  $\log_{10}$  for all comets with measured nickel and iron production rates to-date. Ni, Fe, OH, and CN production rates were taken from Manfroid et al. (2021), Meier et al. (1998), Schleicher & Osip (2002), and Guzik & Drahus (2021). Ratios for 2I/Borisov are indicated by dashed black vertical line, and ratios for Hyakutake are indicated by red dashed lines. Metal/molecule abundance ratios for Hyakutake were derived from the mean of the constrained range of production rate in Hyakutake; for Ni/Fe, ratios derived from the mean production rates and column densities are both shown.

Nickel and iron have been observed in comets of all dynamical families at distances between 0.68 - 3.25 AU. The  $[\text{Ni}/\text{OH}]$  abundance ratio of Hyakutake (-6.56) is most similar to the active Jupiter Family Comet 103P/Hartley 2 ( $[\text{Ni}/\text{OH}] = -6.72$ ) and the dynamically new Oort cloud comet C/2003 K4 (LINEAR) with  $[\text{Ni}/\text{OH}] = -6.68$ . Similarly, the  $[\text{Ni}/\text{CN}]$  ratio (-3.74) is smaller than most of the comets studied by Manfroid et al. (2021) but is again comparable to 103P (-3.79) and C/2003 K4 (-3.96). The presence in 2I/Borisov implies a common organometallic chemistry during planet formation that may be largely independent of dust and volatile formation chemistry given the differences between most solar system comets and the Ni/OH and Ni/CN abundances of 2I/Borisov. The presence in the CO-rich comet C/2016 R2 (PANSTARRS) (McKay et al. 2019) is puzzling considering the production rates of nickel and iron in C/2016 R2 are among the largest to-date. The high metal production and low water production in C/2016 R2, in addition to some comets having enhanced water production from icy grain sublimation, suggests Ni/OH or Ni/H<sub>2</sub>O abundance ratios present a poor categorization of the metallic inventory. It is clear that the magnitudes of nickel and iron production are correlated to overall gas and dust production (Manfroid

et al. 2021), but the driving mechanism behind metal atom production in the coma has yet to be confirmed.

## 5.2. Chemical origins and physical processes

Detection of gas-phase nickel and iron vapor around comets presents a new intersection of chemistry, planetary science, and atomic physics. It is well-known that complex molecules form in planetary disks in the gas phase and on grain surfaces (Öberg et al. 2017), and there are indications that transition metal chemistry is gaining interest, e.g. Kerkeni et al. (2019) and references therein. Both the parent molecule(s) and the excitation process of the atomic metals are currently unknown. However, it is possible to constrain likely parents and production mechanisms considering the totality of metal observations to date.

First we consider the spatial distribution of the nickel and iron emission. Spectra collected at multiple orientations by Manfroid et al. (2021) indicate that the distribution of nickel and iron is isotropic, and the spatial distribution suggests a  $1/r$  profile indicating either direct sublimation from the nucleus or a short-lived parent. We investigated the presence of our Ni and Fe lines from the 0 arcsec spectra in the offset spectra collected at 2, 7, and 10 arcseconds. A’Hearn et al. (2015a) noted several complications in the exact positions of the point-

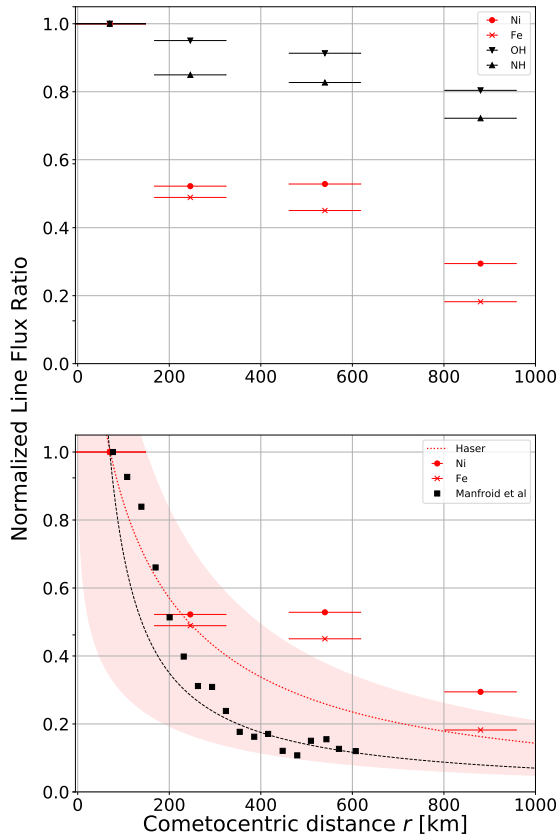


**Figure 9.** (*Top*) Spatial distributions of nickel, iron, and molecular lines normalized to 1 at photocenter. Ni ( $\circ$ ) and Fe ( $\times$ ) flux ratios were taken as the mean of the Ni lines (7) and Fe lines (4) observed at all 4 distances. OH ( $\nabla$ ) and NH ( $\triangle$ ) fluxes and cometocentric distances were digitized from Meier *et al.* (1998). (*Bottom*) Comparison of present Ni and Fe lines to the Fe line profile ( $\blacksquare$ , shifted +70 km) reported in Manfroid *et al.* (2021). A  $1/r$  profile normalized to 1 at  $r = 70$  km is shown in black with grey contours indicating position uncertainty of the 0 arcset pointing of Hyakutake. A Haser model of atomic Ni is shown as a dotted red line, assuming daughter and parent scalelengths of  $8.9 \times 10^5$  km and 200 km and  $Q = 3.45 \times 10^{22} \text{ s}^{-1}$ ; red shaded contours show the uncertainty of the Ni spatial distribution assuming the uncertainty of the photocenter pointing.

ings. The guiding for the Hyakutake spectra was carried out using visible wavelengths, and it is expected that spatial offsets in the UV are likely  $\sim 100$  km larger, with variations of order 10s km within a given spectral range (A’Hearn *et al.* 2015a). While tracking the comet for the 7 arcsec offset observation, a fragment was visually identified and noted in the observing log. We therefore expect emission from the 7 arcsec spectra to

be enhanced from the presence of a localized transient within the field of view (A’Hearn *et al.* 2015a). It is likely that the true spatial offset differs for each offset observation. Therefore, we use these offset spectra only to comment on a qualitative comparison of the spatial distributions.

Fig. 9 (top) shows the spatial distribution of Ni and Fe lines in the present work compared to OH and NH emission from Meier *et al.* (1998). We have assumed the uncertainties in the absolute calibration of the Hyakutake spectra are uniform across the 4 observations, and thus ratios of  $I(r)/I(r = 0)$  are independent of the absolute flux calibration. For each species, we normalized the emission to 1 at  $I(r = 0)$ , which is shown at the expected offset distance in Meier *et al.* (1998), i.e. 70 km. We see large differences between the spatial distributions of Ni and Fe lines compared to the molecular fluxes of OH and NH bands reported in Meier *et al.* (1998). Comparing the molecular and metallic fluxes at 2 and 10 arcseconds, the metal features appear comparatively more enhanced than the molecular features at 7 arcseconds from the presence of the local transient.

Schleicher & Osip (2002) proposed that sublimation of small icy grains in the coma led to enhancement of the water production in Hyakutake. Recently, Sunshine & Feaga (2021) elaborated on the contributions of icy grain sublimation to water vapour around 103P/Hartley, which shows an asymmetric  $\text{H}_2\text{O}$  profile; the differences between water ice and water vapour are clearly distinguishable in imaging from A’Hearn *et al.* (2011). However, the Fe profile reported by Manfroid *et al.* (2021) for 103P was found to be isotropic. If icy grains in the coma contained the Ni and Fe parents, the profiles would be more similar to those observed for e.g. OH and NH. The isotropy of the metal emission and the sharp profiles suggest that the parents of Ni and Fe are not related to icy grain sublimation in the coma.

Fig. 9 (bottom) shows a comparison of the present Ni and Fe flux profiles in Hyakutake (normalized to 1 at  $r = 70$  km) and a Fe profile from 103P/Hartley 2 digitized from Manfroid *et al.* (2021). A  $1/r$  profile (black, blue) and a Haser model (red, assuming daughter and parent lengthscales of  $8.9 \times 10^5$  km and 200 km,  $Q = 3.45 \times 10^{22} \text{ s}^{-1}$ , and a constant outflow velocity given by the assumed relation, cf. Sec. 4.3) are both shown and normalized to 1 at  $r = 70$  km. Ignoring the enhanced fluxes at 7 arcsec (540 km) due to the localized transient, we find reasonable agreement for a simple Haser model with a parent scalelength of order hundreds km, consistent with the assertions of Manfroid *et al.* (2021) and Guzik & Drahus (2021) of a short-lived parent. Without additional insights into the accuracies

of the spatial offsets, a more refined analysis of the spatial distribution in Hyakutake is unreliable.

Two possible parents have been proposed thus far: metal carbonyls, and metal-bonded polycyclic aromatic hydrocarbons (hereafter MBPAHs). Iron and nickel carbonyls ( $\text{Fe}(\text{CO})_5$  and  $\text{Ni}(\text{CO})_4$ ) have been suggested as possible parents by [Manfroid et al. \(2021\)](#), and their chemical model suggests sublimation temperatures in the range 74 - 108 K comparable to CO (81 K), explaining the production of nickel and iron out to several AU. Photochemistry studies of these carbonyls indicate large numbers of charged fragments, including  $\text{Ni}^+$  and  $\text{Fe}^+$  produced by rapid dissociation ([Distefano 1970](#); [Fuss et al. 2001](#); [Cole-Filipiak et al. 2021](#); [Leadbeater 1999](#)). However, photoionization studies involving lasers introduce multiphoton processes wherein multiple CO molecules are progressively stripped from the molecule and the subsequent dissociation produces charged atomic fragments. If successive ionization of the parent is the production pathway, the presence of neutral metals in the coma would require multiple steps (including neutralization) and is at odds with the sharp spatial profiles of the metal emission ([Manfroid et al. 2021](#); [Guzik & Drahus 2021](#)). We are unaware of photoionization experiments carried out using low-intensity sources more akin to the solar radiation field where single-photon excitation is more likely.

The production of neutral fragment(s) from iron carbonyl dissociation have also been studied in electron impact at 50 eV by [Ribar et al. \(2015\)](#). Their apparatus operates in the single collision regime, i.e. only emission from the immediate dissociation and not electron impact excitation of the fragments is observed before the fragments exit the field of view. [Ribar et al. \(2015\)](#) reported emission lines of Fe I from emissive dissociation of iron carbonyl, including the strongest Fe I emission in the spectra of Hyakutake at  $\sim 372$  nm. We have found no comparable spectra in the literature for collision experiments involving nickel carbonyl,  $\text{Ni}(\text{CO})_4$ , but the sizable production of  $\text{Ni}^+$  in photoionization studies suggests similarities to the dissociation of the iron carbonyl. While the spatial profiles of the metal lines in [Manfroid et al. \(2021\)](#) (see Fig. 9) could be explained by prompt emission following dissociation of a parent, i.e. the spectral profiles closely follow the parent distribution, this hypothesis is at odds with the excellent agreement between fluorescence models and observed spectra of nickel and iron in comets. Similarly, the sensitivity to heliocentric velocity (discussed in Sec. 5.3) and the variations in which lines were observed in solar system comets ([Manfroid et al. 2021](#)) strongly validates the assumption of a fluorescent (non-prompt) emission mechanism.

MBPAHs are another promising parent molecule. These molecules have been proposed to exist in the interstellar medium (ISM, see e.g. [Klotz et al. 1996](#)). Transition-metal astrochemistry is an active area of research, and there are indications that metals may play an important role in synthesizing known organic compounds ([Fioroni 2014](#)) and depleting metal abundances (in particular,  $\text{Ni}^+$ ) in the ISM ([Kerkeni et al. 2019](#)). If such MBPAHs were the parent(s), it is possibly detectable by slight frequency shifts induced by metallic ions in the molecular structure, such as the those observed for  $\text{Cu}^+$  ions in quinoline complexes ([Gao et al. 2016](#)). The PAH abundance  $\log_{10}[\text{PAH}/\text{H}_2\text{O}] \approx -6$  ([Klotz et al. 1996](#)) is similar to that of Ni and Fe with respect to water. One can expect that a MBPAH parent, if truly the precursor of gas-phase metals in comae, would most likely be verified by a (cryogenic) sample return mission, or infrared spectroscopy of the parent informed by quantum chemical structure calculations.

Regardless of parent molecule, if the dissociation products ( $\text{Ni}^+$ ,  $\text{Fe}^+$ ) were ionic the fragments would need to neutralize via charge exchange or radiative/dielectronic capture within a distance much smaller than 1000 km to explain the observed spatial profiles in [Manfroid et al. \(2021\)](#) and [Guzik & Drahus \(2021\)](#). Capture of a free electron to produce neutral metal atoms is unlikely provided the low electron densities in the inner coma, c.f.  $n_e \leq 10^3$  at 67P ([Myllys, M. et al. 2019](#)). Ion impact experiments of iron carbonyl ([Indrajith et al. 2019](#)) indicate  $\text{Fe}^+$  energies post-fragmentation between 0.1 - 1 eV (0.6 - 1.9 km/s). At these low energies the cross section for charge exchange is likely small,  $< 10^{-17}$  cm<sup>2</sup> (see [Friedman & DuCharme \(2017\)](#) and references therein). For a nominal neutral density in the inner coma of  $10^{10}$  cm<sup>-3</sup>, the mean free path for charge exchange is in order  $10^4$  km, too large to explain the observed spatial profiles. In total, a production mechanism involving collisions with  $\text{H}_2\text{O}$  or electrons which neutralize or produce charged fragments is unlikely.

### 5.3. Sensitivity to Heliocentric Velocity

We investigated the sensitivity of the fluorescence efficiencies of our observed Ni and Fe lines to heliocentric velocity. Fig. 10 shows the calculated fluorescence efficiencies for  $r_h = 1$  AU for 5 observed lines of Ni I (top) and Fe I (bottom) as a function of heliocentric velocity; calculated fluorescence efficiencies for all of our observed metal lines are available in Appendix A. [Manfroid et al. \(2021\)](#) noted that the metal fluorescence efficiencies are sensitive to heliocentric velocity as the driving fluxes for many of the metal emission lines reside at or near absorption features in the solar spectrum. In Fig. 10, as  $v_h$

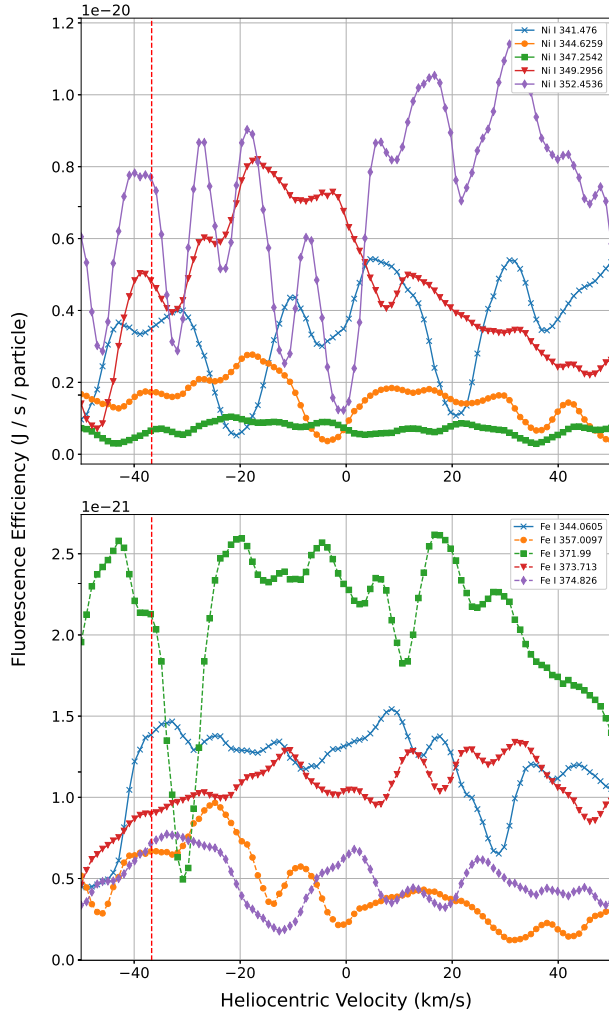


**Figure 10.** Sensitivity of our modeled fluorescence efficiencies of some representative Ni I lines (top) and Fe I lines (bottom) to heliocentric velocity. Efficiencies were calculated for a heliocentric distance of 1 AU. The heliocentric velocity of Hyakutake (-36.7 km/s) is shown as a vertical dashed line.

changes the spectral location of the driving flux sweeps over absorption features for e.g. Ni I 352.45 nm. Within the range of  $v_h = \pm 50$  km/s, the fluorescence efficiencies typically vary by a factor of 3. These changes are comparable to the velocity sensitivity of molecular emission, e.g. a factor of 2 for the NH A-X 0-0 band in the range  $v_h = \pm 80$  km/s (Meier *et al.* 1998) and a factor of 4 for OH A-X 0-0 across  $v_h = \pm 60$  km/s (Schleicher & A’Hearn 1988).

Considering the excellent agreement between fluorescence-modeled and observed line intensities of these atomic metal emissions, a prompt emissive origin is unlikely but not disproven. Prompt emission is most sensitive to UV flux (Leadbeater 1999), whereas fluorescence is particularly sensitive to heliocentric velocity.

The ratio of two lines, one strongly sensitive to  $v_h$  and one insensitive to  $v_h$ , would allow for confirmation of a definitive fluorescence mechanism. Two potential line ratios for this purpose would be Ni I  $I(352.54)/I(347.25)$  or Fe I  $I(371.99)/I(374.83)$ . Any line ratio involving Fe I 371.99 nm line is favorable for this test as the 371.99 nm line is among the strongest iron features (cf. the line list of Manfroid *et al.* 2021<sup>6</sup>) and presents significant sensitivity to heliocentric velocities around -30 km/s.

## 6. SUMMARY

We developed a many-level fluorescence model compatible with atomic data in the NIST ASD (Kramida *et al.* 2020). The code is made publicly available with documentation and sample files at the author’s github page. Test calculations on a grid of heliocentric velocities show that atomic metal emission for constant production is sensitive to heliocentric velocity.

Using our fluorescence model, we re-analyzed archived data of the 1996 apparition of comet Hyakutake. The nucleus-centered spectra of Hyakutake were compared against synthetic fluorescence spectra of atomic metals and spectra of a Ni-Fe laboratory plasma. We identified 14 emission lines of Ni I and 23 lines of Fe I. Agreement between the modeled and fluorescence spectra of Ni I and Fe I is achieved within a factor of  $\sim 2$  on average. Using our model, we validated the detections of iron and nickel atoms in cometary atmospheres reported for solar system comets (Manfroid *et al.* 2021) and 2I/Borisov (Guzik & Drahus 2021). The observed lines are E1-allowed transitions from excited odd configurations to the ground and metastable even-parity configurations. The spatial distribution of metal emission mimics that observed for other comets and appears to fall off sharply compared to molecular features in the same spectra.

Assuming fluorescence emission, we derived column densities of nickel and iron atoms, from which we used the total number of particles within our aperture to inform Haser models to estimate the production rates  $Q_{\text{Ni}} = 2.6 - 4.1 \times 10^{22} \text{ s}^{-1}$  and  $Q_{\text{Fe}} = 0.4 - 2.6 \times 10^{23} \text{ s}^{-1}$ . Using our derived column densities the Ni/Fe abundance ratio  $\log_{10}[\text{Ni}/\text{Fe}] = -0.38 \pm 0.06$  differs significantly from abundances observed for the sun, Ikeya-Seki, and in-situ measurements of 1P/Halley. Our ratios are in-line with those observed in other solar system comets and 2I/Borisov. Comparison of the observed flux profiles to molecular features in Hyakutake and metal pro-

<sup>6</sup> Line list available as supplementary information at <https://www.researchsquare.com/article/rs-101492/v1>

files from 103P/Hartley 2 suggest a near-nucleus source of the atomic metals. Combined, our findings therefore support a short-lived parent molecule with a fluorescence emission mechanism.

In summary, we now have several clues as to the production and emission mechanisms:

- Surface brightness profiles with respect to cometocentric distances in Hyakutake and 103P are sharp compared to non-prompt OH and NH emission. These steep profiles in the active comets C/1996 B2 (Hyakutake) and the comet sample of [Manfroid et al. \(2021\)](#) suggest the source of Ni and Fe is likely independent of icy grain activity. Abundance comparisons to H<sub>2</sub>O and/or OH are poor for categorizing the metallic inventory of the coma.
- The sharpness of the spatial profiles suggest either direct sublimation from the nucleus, a short-lived parent, or a emissive dissociation (prompt) process. Temperatures are insufficient for sublimating iron and nickel metal directly, and the abundance ratio [Ni/Fe] suggests a non-dust source.
- The emission of iron and nickel atoms is well described by fluorescence models, and we find no evidence for emission from highly-excited levels expected populated by emissive dissociation. This assertion is reinforced by the strong sensitivity to heliocentric velocity and variety in observed metal lines to-date. Line ratios of  $v_h$ -sensitive/ $v_h$ -insensitive lines would indicate the correct emission mechanism.

- Photoionization studies of the suggested parents Ni(CO)<sub>4</sub> and Fe(CO)<sub>5</sub> involved multiphoton processes that produced the ionic fragments Ni<sup>+</sup> and Fe<sup>+</sup>. Densities of both electrons and neutrals in the coma are insufficient for neutralizing charged fragments, and no Ni II or Fe II emission has been observed. It is unclear if single-photon processes are capable of inducing dissociation of iron and nickel carbonyls over the small distances required.
- PAH abundances (with respect to water) are of similar magnitude to nickel and iron, suggesting a possible metal-bonded polycyclic aromatic hydrocarbon parent. Experiments on Cu<sup>+</sup> bonded to PAHs in the literature yielded observable differences in IR spectra; a similar effect is presumably possible for the parents of atomic nickel and iron.

The surprise discoveries of Ni I and Fe I emission in comets ([Manfroid et al. 2021](#); [Guzik & Drahus 2021](#)) have elucidated a new diagnostic to cometary scientists in which some information on the organo-metallic inventories of comets can be probed without waiting for rare sungrazer events or sample return missions. Given the propensity of nickel and iron emission in the UV-VIS-NIR range, these lines may be analyzed alongside typical molecular features. With sufficient sampling, these discoveries may shed light on aspects of as-yet-unexplored organic astrochemistry.

**Table 2.** List of Observed Ni I and Fe I Lines. All wavelengths are reported as nm in standard air. Intensities are in units of  $10^{-24} \text{ J s}^{-1} \text{ cm}^{-2}$ ; model intensities are shown after scaling by the geocentric distance, aperture size, and derived column densities. Einstein  $A$  values are written as  $m + n \equiv m \times 10^n$ . Lines previously observed in solar system comets (SS, Manfroid *et al.* 2021), 2I/Borisov (BOR, Guzik & Drahus 2021), or Ikeya-Seki (IS, Preston 1967; Slaughter 1969) are shown by a ‘ $\mathcal{C}$ ’ symbol. Unknown LS term identifications for a given J-level are indicated by a ? symbol.

Species	$\lambda_{\text{Ritz}}$	$\lambda_{\text{comet}}$	$\lambda_{\text{lab}}$	$I_{\text{comet}}$	$I_{\text{model}}$	A Value	Lower Level	Upper Level	Confidence	SS	BOR	IS
Fe I	344.06	344.07	344.15	38.6±15.44	236.89±18.68	1.7+07	$3d^6 4s^2 a^5 D_4$	$3d^6(^5D)4s4p(^3P) w^5 P_3$	A (Bl. Lab)	✓		✓
Fe I	344.1	344.11	344.15	18.5±7.4	89.1±7.55	1.2+07	$3d^6 4s^2 a^5 D_3$	$3d^6(^5D)4s4p(^3P) w^5 P_2$	A (Bl. Lab)	✓		✓
Fe I	346.59	346.6		24.3±9.72	71.43±6.02	1.2+07	$3d^6 4s^2 a^5 D_1$	$3d^6(^5D)4s4p(^3P) z^5 P_1$	B (OH)	✓		✓
Fe I	349.06	349.07		24.6±9.84	83.84±5.03	6.1+06	$3d^6 4s^2 a^5 D_3$	$3d^6(^5D)4s4p(^3P) z^5 P_3$	A	✓		✓
Fe I	356.54	356.55	356.51	47.6±19.04	51.11±2.82	4.3+07	$3d^7(^4F)4s a^5 F_3$	$3d^7(^4F)4p z^3 G_4$	C	✓		✓
Fe I	357.01	357.02		53.6±21.44	113.57±2.8	6.8+07	$3d^7(^4F)4s a^5 F_4$	$3d^7(^4F)4p w^3 G_5$	A	✓		✓
Fe I	358.12	358.13		84.7±33.88	107.83±3.53	1.0+08	$3d^7(^4F)4s a^5 F_5$	$3d^7(^4F)4p w^5 G_6$	B (CN)	✓		✓
Fe I	364.78	364.81		69.6±27.84	61.15±1.46	2.9+07	$3d^7(^4F)4s a^5 F_4$	$3d^7(^4F)4p z^5 G_5$	B (CH)	✓		✓
Fe I	371.99	372.01	372.0	407.0±162.8	361.05±8.0	1.6+07	$3d^6 4s^2 a^5 D_4$	$3d^6(^5D)4s4p(^3P) w^5 F_5$	B (NH)	✓		✓
Fe I	372.26	372.28	373.49	22.0±8.8	66.16±1.58	5.0+06	$3d^6 4s^2 a^5 D_2$	$3d^6(^5D)4s4p(^3P) z^5 F_2$	A	✓		✓
Fe I	373.49	373.51	373.69	101.0±40.4	60.6±1.14	9.0+07	$3d^7(^4F)4s a^5 F_5$	$3d^7(^4F)4p y^5 F_5$	B (NH)	✓		✓
Fe I	373.71	373.74		155.0±62.0	153.2±2.6	1.4+07	$3d^6 4s^2 a^5 D_3$	$3d^6(^5D)4s4p(^3P) w^5 F_4$	A	✓		✓
Fe I	374.83	374.85		44.8±17.92	120.96±2.46	9.2+06	$3d^6 4s^2 a^5 D_1$	$3d^6(^5D)4s4p(^3P) w^5 F_2$	C (NH)	✓		✓
Fe I	374.95	374.98	374.95	141.0±56.4	99.4±2.66	7.6+07	$3d^7(^4F)4s a^5 F_4$	$3d^7(^4F)4p y^5 F_4$	B (NH)	✓		✓
Fe I	375.82	375.85	375.78	46.4±18.56	110.12±2.83	6.3+07	$3d^7(^4F)4s a^5 F_3$	$3d^7(^4F)4p y^5 F_3$	A	✓		✓
Fe I	379.5	379.51		16.0±6.4	19.78±0.47	1.2+07	$3d^7(^4F)4s a^5 F_2$	$3d^7(^4F)4p y^5 F_3$	A	✓		✓
Fe I	381.3	381.3		14.3±5.72	12.67±0.26	7.9+06	$3d^7(^4F)4s a^5 F_3$	$3d^6(^5D)4s4p(^3P) z^3 P_2$	A	✓		✓
Fe I	382.04	382.06	382.05	111.0±44.4	115.8±2.86	6.8+07	$3d^7(^4F)4s a^5 F_5$	$3d^7(^4F)4p y^5 D_4$	A	✓		✓
Fe I	382.44	382.45		34.5±13.8	45.7±0.97	2.8+06	$3d^6 4s^2 a^5 D_4$	$3d^6(^5D)4s4p(^3P) z^5 D_3$	A	✓		✓
Fe I	382.59	382.6	382.58	63.3±25.32	126.67±2.18	6.0+07	$3d^7(^4F)4s a^5 F_4$	$3d^7(^4F)4p y^5 D_3$	A	✓		✓
Fe I	383.42	383.43	383.42	37.0±14.8	82.96±1.85	4.5+07	$3d^7(^4F)4s a^5 F_3$	$3d^7(^4F)4p y^5 D_2$	A	✓		✓
Fe I	384.04	384.06	384.08	41.4±16.56	55.67±1.22	4.7+07	$3d^7(^4F)4s a^5 F_2$	$3d^7(^4F)4p y^5 D_1$	A	✓		✓
Fe I	385.99	386.0	385.99	502.0±200.8	87.65±1.54	9.7+06	$3d^6 4s^2 a^5 D_4$	$3d^6(^5D)4s4p(^3P) z^5 D_4$	C (CN)	✓		✓
Ni I	323.29	323.31	323.35	153.0±61.2	50.53±7.75	7.3+06	$3d^8(^3F)4s^2(^3F_4)$	$3d^8(^3F)4s4p(^3P)(^3G_5)$	A	✓		✓
Ni I	339.1	339.13	339.09	34.6±13.84	29.7±5.69	6.6+06	$3d^8(^3F)4s^2(^3F_4)$	$3d^9(^2D)4p^3 F_4$	B (NH)	✓		✓

**Table 2** continued

Table 2 (continued)

Species	$\lambda_{\text{Ritz}}$	$\lambda_{\text{comet}}$	$\lambda_{\text{lab}}$	$I_{\text{comet}}$	$I_{\text{model}}$	A Value	Lower Level	Upper Level	Confidence	SS	BOR	IS
Ni I	339.3	339.32	339.27	232.0±92.8	96.16±12.59	2.4+07	$3d^9(^2D)4s(^3D_3)$	$3d^9(^2D)4p(^? )_3$	B (NH)	✓	✓	✓
Ni I	341.48	341.49	341.46	494.0±197.6	245.79±33.2	5.5+07	$3d^9(^2D)4s(^3D_3)$	$3d^9(^2D)4p(^3F_4)$	A	✓	✓	✓
Ni I	343.36	343.37	343.33	101.0±40.4	40.69±5.51	1.7+07	$3d^9(^2D)4s(^3D_3)$	$3d^9(^2D)4p(^3F_3)$	A	✓		✓
Ni I	343.73	343.74	343.71	49.2±19.68	17.4±3.05	4.4+06	$3d^8(^3F)4s(^3F_4)$	$3d^8(^3F)4s4p(^3P)(^5F_4)$	A	✓		✓
Ni I	344.63	344.64	344.61	106.0±42.4	121.58±17.87	4.4+07	$3d^9(^2D)4s(^3D_2)$	$3d^9(^2D)4p(^3D_2)$	A	✓	✓	✓
Ni I	345.85	345.86	345.82	153.0±61.2	84.76±11.62	6.1+07	$3d^9(^2D)4s(^3D_1)$	$3d^9(^2D)4p(^3F_2)$	A	✓	✓	✓
Ni I	346.17	346.18	346.14	291.0±116.4	106.02±12.26	2.7+07	$3d^9(^2D)4s(^3D_3)$	$3d^8(^3F)4s4p(^3P)(^5F_4)$	A	✓	✓	✓
Ni I	347.25	347.27	347.23	93.5±37.4	46.98±5.82	1.2+07	$3d^9(^2D)4s(^3D_2)$	$3d^9(^2D)4p(^? )_3$	A	✓		✓
Ni I	349.3	349.31		125.0±50.0	335.71±42.69	9.8+07	$3d^9(^2D)4s(^3D_2)$	$3d^9(^2D)4p(^3P_1)$	A	✓	✓	✓
Ni I	351.51	351.52	351.48	176.0±70.4	98.19±13.79	4.2+07	$3d^9(^2D)4s(^3D_2)$	$3d^9(^2D)4p(^3F_3)$	A	✓	✓	✓
Ni I	352.45	352.47	352.43	388.0±155.2	539.61±86.29	1.0+08	$3d^9(^2D)4s(^3D_3)$	$3d^9(^2D)4p(^3P_2)$	A	✓	✓	✓
Ni I	361.94	361.95	361.9	109.0±43.6	46.51±5.2	6.6+07	$3d^9(^2D)4s(^1D_2)$	$3d^9(^2D)4p(^1F_3)$	A	✓	✓	✓

*Software:* Python3, NumPy (Harris *et al.* 2020), SciPy (Virtanen *et al.* 2020), Small Body Python (sbpy, Mommert *et al.* 2019)

## ACKNOWLEDGMENTS

Many thanks are extended to John Noonan (Lunar and Planetary Lab, U. Arizona) for his helpful discussions during the development of the fluorescence model. The authors gratefully acknowledge funding support from the National Science Foundation (grant Nos. 1815833, 1815932, and 1816984. The Compact Toroidal Hybrid measurements were supported by U.S. DOE Grant No. DE-FG-02-00ER54610. We are grateful for the support of the Auburn University Hopper Cluster for their assistance and computing resources utilized for this work. We extend a special thank you to the observing team (A’Hearn *et al.* 2015b) for collecting and archiving their data through the Planetary Data System, and the NIST ASD team for acquiring, compiling, and archiving useful atomic data.

## REFERENCES

- A’Hearn, M. F., Millis, R. C., Schleicher, D. G., Osip, D. J., & Birch, P. V. 1995, *Icarus*, 118, 223, doi: <https://doi.org/10.1006/icar.1995.1190>
- A’Hearn, M. F., Swamy, K. S. K., Wellnitz, D. D., & Meier, R. 2015a, *The Astronomical Journal*, 150, 5
- A’Hearn, M. F., Wellnitz, D. D., & Meier, R. 2013, *Proceedings of the International Astronomical Union*, 9, 216–218, doi: [10.1017/S1743921313015883](https://doi.org/10.1017/S1743921313015883)
- . 2015b, NASA Planetary Data System, urn:nasa:pds:gbo-kpno:hyakutake\_spectra::1.0
- A’Hearn, M. F., Belton, M. J. S., Delamere, W. A., *et al.* 2011, *Science*, 332, 1396, doi: [10.1126/science.1204054](https://doi.org/10.1126/science.1204054)
- Altwegg, K., Balsiger, H., & Fuselier, S. A. 2019, *Annual Review of Astronomy and Astrophysics*, 57, 113, doi: [10.1146/annurev-astro-091918-104409](https://doi.org/10.1146/annurev-astro-091918-104409)
- Berger, E. L., Zega, T. J., Keller, L. P., & Lauretta, D. S. 2011, *Geochimica et Cosmochimica Acta*, 75, 3501, doi: <https://doi.org/10.1016/j.gca.2011.03.026>
- Bockelée-Morvan, D., & Biver, N. 2017, *Philosophical Transactions of the Royal Society A: Mathematical, Physical and Engineering Sciences*, 375, 20160252, doi: [10.1098/rsta.2016.0252](https://doi.org/10.1098/rsta.2016.0252)
- Bodewits, D., Orszagh, J., Noonan, J., Āurian, M., & Matejčĭk, v. 2019, *Astrophysical Journal*, 885, 167, doi: [10.3847/1538-4357/ab43c9](https://doi.org/10.3847/1538-4357/ab43c9)
- Bromley, S. J., Johnson, C. A., Ennis, D. A., *et al.* 2020, *The Astrophysical Journal Supplement Series*, 250, 19, doi: [10.3847/1538-4365/abaa4d](https://doi.org/10.3847/1538-4365/abaa4d)
- Brownlee, D. 2014, *Annual Review of Earth and Planetary Sciences*, 42, 179, doi: [10.1146/annurev-earth-050212-124203](https://doi.org/10.1146/annurev-earth-050212-124203)
- Chance, K., & Kurucz, R. 2010, *Journal of Quantitative Spectroscopy and Radiative Transfer*, 111, 1289, doi: <https://doi.org/10.1016/j.jqsrt.2010.01.036>
- Cochran, A. L., & Schleicher, D. G. 1993, *Icarus*, 105, 235, doi: [10.1006/icar.1993.1121](https://doi.org/10.1006/icar.1993.1121)
- Cole-Filipiak, N. C., Troß, J., Schrader, P., McCaslin, L. M., & Ramasesha, K. 2021, *The Journal of Chemical Physics*, 154, 134308, doi: [10.1063/5.0041074](https://doi.org/10.1063/5.0041074)
- Cremonese, G., Huebner, W., Rauer, H., & Boice, D. 2002, *Advances in Space Research*, 29, 1187, doi: [https://doi.org/10.1016/S0273-1177\(02\)00136-9](https://doi.org/10.1016/S0273-1177(02)00136-9)
- Crismani, M. M. J., Schneider, N. M., Evans, J. S., *et al.* 2018, *Journal of Geophysical Research: Planets*, 123, 2613, doi: [10.1029/2018je005750](https://doi.org/10.1029/2018je005750)
- Distefano, G. 1970, *Journal of research of the National Bureau of Standards. Section A, Physics and chemistry*, 74A, 233, doi: [10.6028/jres.074A.019](https://doi.org/10.6028/jres.074A.019)

- Feldman, P. D., Cochran, A. L., & Combi, M. R. 2004, Spectroscopic investigations of fragment species in the coma, ed. M. C. Festou, H. U. Keller, & H. A. Weaver, 425
- Fernando, A. M., Bernath, P. F., Hodges, J. N., & Masseron, T. 2018, *Journal of Quantitative Spectroscopy and Radiative Transfer*, 217, 29, doi: <https://doi.org/10.1016/j.jqsrt.2018.05.021>
- Festou, M. C. 1981, *A&A*, 95, 69
- Fioroni, M. 2014, *Phys. Chem. Chem. Phys.*, 16, 24312, doi: [10.1039/C4CP03218G](https://doi.org/10.1039/C4CP03218G)
- Friedman, B., & DuCharme, G. 2017, *Journal of Physics B: Atomic, Molecular and Optical Physics*, 50, 115202, doi: [10.1088/1361-6455/aa6cce](https://doi.org/10.1088/1361-6455/aa6cce)
- Fuss, W., Schmid, W. E., & Trushin, S. A. 2001, *The Journal of Physical Chemistry A*, 105, 333, doi: [10.1021/jp002276z](https://doi.org/10.1021/jp002276z)
- Gao, J., Bouwman, J., Berden, G., & Oomens, J. 2016, *The Journal of Physical Chemistry A*, 120, 7800, doi: [10.1021/acs.jpca.6b05060](https://doi.org/10.1021/acs.jpca.6b05060)
- Guzik, P., & Drahus, M. 2021, *Nature*, 593, 375, doi: [10.1038/s41586-021-03485-4](https://doi.org/10.1038/s41586-021-03485-4)
- Harris, C. R., Millman, K. J., van der Walt, S. J., et al. 2020, *Nature*, 585, 357, doi: [10.1038/s41586-020-2649-2](https://doi.org/10.1038/s41586-020-2649-2)
- Hartwell, G., Knowlton, S., Hanson, J., Ennis, D., & Maurer, D. 2017, *Fusion Science and Technology*, 72, 76, doi: [10.1080/15361055.2017.1291046](https://doi.org/10.1080/15361055.2017.1291046)
- Haser, L., Oset, S., & Bodewits, D. 2020, *The Planetary Science Journal*, 1, 83, doi: [10.3847/psj/abc17b](https://doi.org/10.3847/psj/abc17b)
- Huebner, W., & Mukherjee, J. 2015, *Planetary and Space Science*, 106, 11, doi: <https://doi.org/10.1016/j.pss.2014.11.022>
- Indrajith, S., Rousseau, P., Huber, B. A., et al. 2019, *The Journal of Physical Chemistry C*, 123, 10639, doi: [10.1021/acs.jpcc.9b00289](https://doi.org/10.1021/acs.jpcc.9b00289)
- Jessberger, E. K., Christoforidis, A., & Kissel, J. 1988, *Nature*, 332, 691, doi: [10.1038/332691a0](https://doi.org/10.1038/332691a0)
- Johnson, C. A., Ennis, D. A., Loch, S. D., et al. 2019, *Plasma Physics and Controlled Fusion*, 61, 095006, doi: [10.1088/1361-6587/ab2b25](https://doi.org/10.1088/1361-6587/ab2b25)
- Jones, G. H., Knight, M. M., Battams, K., et al. 2017, *Space Science Reviews*, 214, 20, doi: [10.1007/s11214-017-0446-5](https://doi.org/10.1007/s11214-017-0446-5)
- Kerkeni, B., Aquino, A. J. A., Berman, M. R., & Hase, W. L. 2019, *Molecular Physics*, 117, 1392, doi: [10.1080/00268976.2018.1552800](https://doi.org/10.1080/00268976.2018.1552800)
- Kim, S. J., A'Hearn, M., Wellnitz, D., Meier, R., & Lee, Y. 2003, *Icarus*, 166, 157, doi: <https://doi.org/10.1016/j.icarus.2003.07.003>
- Klotz, A., Marty, P., Boissel, P., et al. 1996, *Planetary and Space Science*, 44, 957, doi: [10.1016/0032-0633\(96\)00026-8](https://doi.org/10.1016/0032-0633(96)00026-8)
- Kovačević, J., Popović, L. Č., & Dimitrijević, M. S. 2010, *The Astrophysical Journal Supplement Series*, 189, 15, doi: [10.1088/0067-0049/189/1/15](https://doi.org/10.1088/0067-0049/189/1/15)
- Kramida, A., Yu. Ralchenko, Reader, J., & and NIST ASD Team. 2020, NIST Atomic Spectra Database (ver. 5.8), [Online]. Available: <https://physics.nist.gov/asd> [2016, January 31]. National Institute of Standards and Technology, Gaithersburg, MD.
- Kurucz, R., & Bell, B. 1995, *Atomic Line Data* (R.L. Kurucz and B. Bell) Kurucz CD-ROM No. 23. Cambridge, 23
- Kurucz, R. L., Furenlid, I., Brault, J., & Testerman, L. 1984, *Solar flux atlas from 296 to 1300 nm*
- Leadbeater, N. 1999, *Coordination Chemistry Reviews*, 188, 35, doi: [10.1016/s0010-8545\(98\)00217-3](https://doi.org/10.1016/s0010-8545(98)00217-3)
- Manfroid, J., Hutsemékers, D., & Jehin, E. 2021, *Nature*, 593, 372, doi: [10.1038/s41586-021-03435-0](https://doi.org/10.1038/s41586-021-03435-0)
- McKay, A. J., DiSanti, M. A., Kelley, M. S. P., et al. 2019, *The Astronomical Journal*, 158, 128, doi: [10.3847/1538-3881/ab32e4](https://doi.org/10.3847/1538-3881/ab32e4)
- Meier, R., Wellnitz, D., Kim, S. J., & A'Hearn, M. F. 1998, *Icarus*, 136, 268, doi: [10.1006/icar.1998.6022](https://doi.org/10.1006/icar.1998.6022)
- Mommert, M., p. Kelley, M. S., de Val-Borro, M., et al. 2019, *Journal of Open Source Software*, 4, 1426, doi: [10.21105/joss.01426](https://doi.org/10.21105/joss.01426)
- Morton, D. C. 2000, *The Astrophysical Journal Supplement Series*, 130, 403, doi: [10.1086/317349](https://doi.org/10.1086/317349)
- Myllys, M., Henri, P., Galand, M., et al. 2019, *A&A*, 630, A42, doi: [10.1051/0004-6361/201834964](https://doi.org/10.1051/0004-6361/201834964)
- Nierenberg, A. M., Gilman, D., Treu, T., et al. 2019, *Monthly Notices of the Royal Astronomical Society*, 492, 5314, doi: [10.1093/mnras/stz3588](https://doi.org/10.1093/mnras/stz3588)
- Pollack, J. B., Hollenbach, D., Beckwith, S., et al. 1994, *ApJ*, 421, 615, doi: [10.1086/173677](https://doi.org/10.1086/173677)
- Preston, G. W. 1967, *ApJ*, 147, 718, doi: [10.1086/149049](https://doi.org/10.1086/149049)
- Ribar, A., Danko, M., Országh, J., et al. 2015, *The European Physical Journal D*, 69, 117, doi: [10.1140/epjd/e2015-50755-x](https://doi.org/10.1140/epjd/e2015-50755-x)
- Roos-Serote, M., Barucci, A., Crovisier, J., et al. 1995, *Geophysical Research Letters*, 22, 1621, doi: <https://doi.org/10.1029/95GL00809>
- Rubin, M., Altwegg, K., Balsiger, H., et al. 2019, *Monthly Notices of the Royal Astronomical Society*, 489, 594, doi: [10.1093/mnras/stz2086](https://doi.org/10.1093/mnras/stz2086)
- Schleicher, D. G., & A'Hearn, M. F. 1988, *ApJ*, 331, 1058, doi: [10.1086/166622](https://doi.org/10.1086/166622)

- Schleicher, D. G., & Osip, D. J. 2002, *Icarus*, 159, 210, doi: <https://doi.org/10.1006/icar.2002.6875>
- Slaughter, C. D. 1969, *AJ*, 74, 929, doi: [10.1086/110884](https://doi.org/10.1086/110884)
- Strøm, P. A., Bodewits, D., Knight, M. M., et al. 2020, *Publications of the Astronomical Society of the Pacific*, 132, 101001, doi: [10.1088/1538-3873/aba6a0](https://doi.org/10.1088/1538-3873/aba6a0)
- Sunshine, J. M., & Feaga, L. M. 2021, *The Planetary Science Journal*, 2, 92, doi: [10.3847/psj/abf11f](https://doi.org/10.3847/psj/abf11f)
- Villanueva, G., Smith, M., Protopapa, S., Faggi, S., & Mandell, A. 2018, *Journal of Quantitative Spectroscopy and Radiative Transfer*, 217, 86, doi: <https://doi.org/10.1016/j.jqsrt.2018.05.023>
- Virtanen, P., Gommers, R., Oliphant, T. E., et al. 2020, *Nature Methods*, 17, 261, doi: [10.1038/s41592-019-0686-2](https://doi.org/10.1038/s41592-019-0686-2)
- Wyckoff, S., Heyd, R. S., & Fox, R. 1999, *Astrophysical Journal*, 512, L73, doi: [10.1086/311869](https://doi.org/10.1086/311869)
- Öberg, K. I., Guzmán, V. V., Merchantz, C. J., et al. 2017, *The Astrophysical Journal*, 839, 43, doi: [10.3847/1538-4357/aa689a](https://doi.org/10.3847/1538-4357/aa689a)

APPENDIX

A. FLUORESCENCE EFFICIENCIES OF OBSERVED METAL LINES

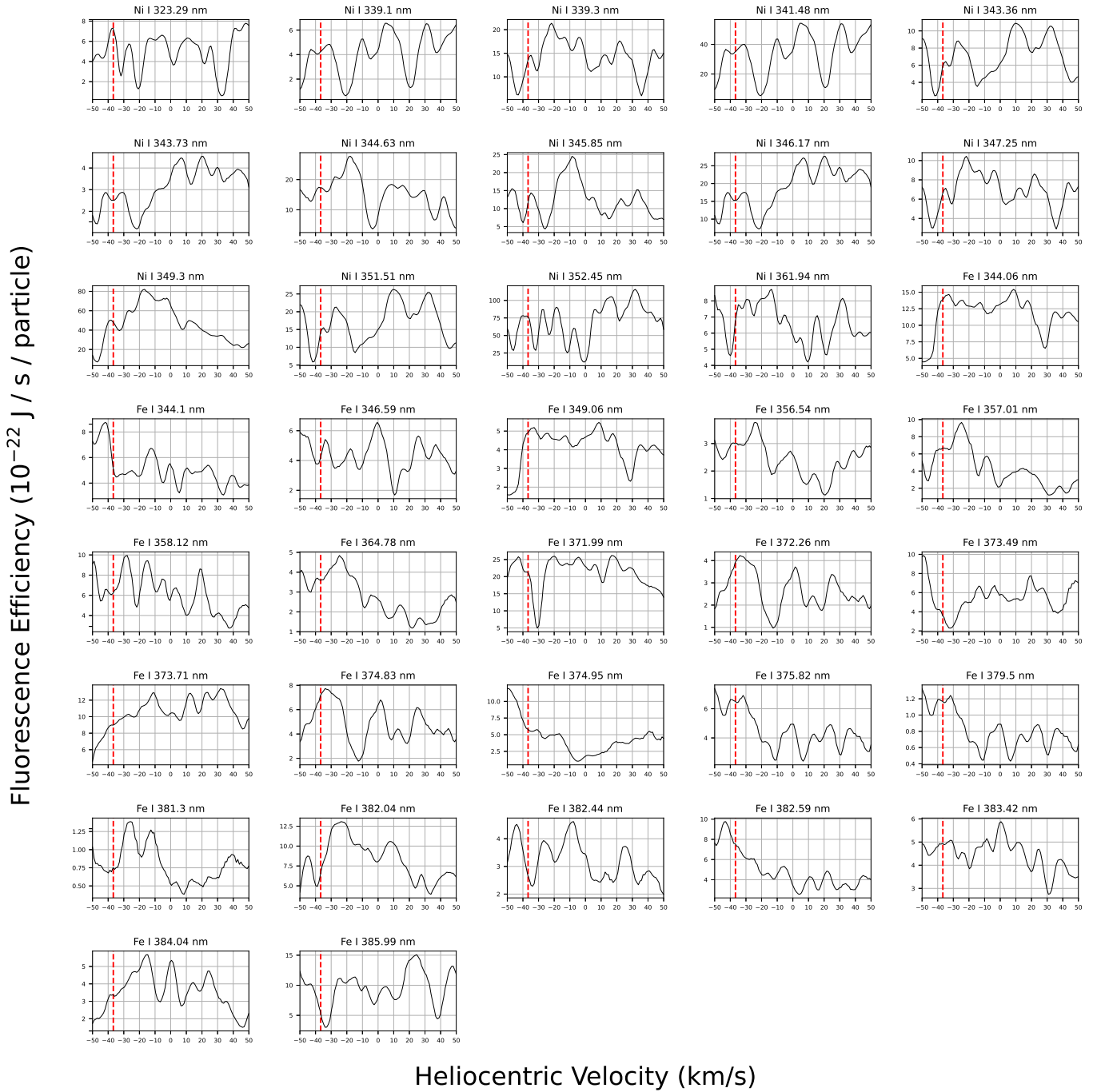


**Figure 11.** Calculated fluorescence efficiencies for observed metal lines in Hyakutake as a function of heliocentric velocity. The velocity of Hyakutake ( $-36.7$  km/s) is indicated by a vertical red line in each plot.